August 2021

Master's Thesis

Preparation and Characterization of Highly Porous Biocarbons from Giant *Miscanthus* for Capacitive Deionization

Graduate School of Chosun University

Department of Chemical Engineering

Yeong-Pil Lee

Preparation and Characterization of Highly Porous Biocarbons from Giant *Miscanthus* for Capacitive Deionization

축전식 이온 제거를 위한 거대억새 유래
다공성 바이오탄소의 제조 및 특성 평가

August 27, 2021

Graduate School of Chosun University

Department of Chemical Engineering

Yeong-Pil Lee

Preparation and Characterization of Highly Porous Biocarbons from Giant *Miscanthus* for Capacitive Deionization

Supervised by Professor Jae-Wook Lee

A thesis submitted in partial fulfillment of the requirements for the Degree of Master in Engineering

April 2021

Graduate School of Chosun University

Department of Chemical Engineering

Yeong-Pil Lee

Approval of the thesis for
Yeong-Pil Lee

Committee Chair	Chosun University	Ph.D./Prof. Jung Heon Lee
Committee	Chosun University	Ph.D./Prof. Jung-Soo Lee
Committee	Chosun University	Ph.D./Prof. Jae-Wook Lee

May 2021

Graduate School of Chosun University

CONTENTS

LIST OF TABLES

LIST OF FIGURES

ABSTRACT

Preparation and Characterization of Highly Porous Biocarbons from Giant *Miscanthus* for Capacitive Deionization

Yeong-Pil Lee

Advisor : Ph.D./Prof. Jae-Wook Lee

Department of Chemical Engineering

Graduate School of Chosun University

Biomass resources including tamarind shell, date seed, pinecone, citrus peel, soybean shell, almond shell, spent coffee ground, rice husk, coconut shell, olive seed and wheat straw have been recently used for the preparation of porous biocarbons through carbonization and activation processes. Compared to coal-based activated carbons, biocarbons appear to be new potential cost-effective and environmentally-friendly carbon materials with great application of water pollution treatment, CO_2 capture, energy storage, electrochemical sensing, catalysis and capacitive deionization.

In this study, porous biocarbons with high specific surface area and narrow pore size distribution were successfully prepared from giant *Miscanthus* (GM). The activation was conducted by a simple one-step process involving $ZnCl_2$ impregnation because of relatively low activation temperature, limitation of tar and improvement of surface hydrophilicity. The ratio of $ZnCl_2$/GM (1, 2, 4) and activation temperatures (600, 700, 800 °C) were optimized based on the specific capacitance and salt adsorption capacity. Many instrumental analyses of TGA, SEM, BET, XRD, Raman and FTIR were employed for the evaluation of physical and chemical properties, surface morphology, specific surface area, pore size distribution and crystallinity. The specific surface area and mean pore size of the porous biocarbons under different activation conditions were

in the range of 994 – 1661 m^2 g^{-1} and about 2 nm, respectively. Nitrogen adsorption and desorption isotherms were type I according to the IUPAC classification. The intensity ratio of D band/G band indicating the development of surface roughness and pore structures increased with $ZnCl_2$/GM and activation temperatures. On the other hand, the electrochemical properties were measured by cyclic voltammetry, chronoamperometry and electrochemical impedance spectroscopy. The specific capacitances of cyclic voltammetry were in the range of 167 – 228 F g^{-1} at 5 mV s^{-1} of scan rate. The adsorption and desorption behaviors showed excellent reproducibility under key operating conditions of flow rate, NaCl concentration and applied potential. The maximum salt adsorption capacity was 21.9 mg g^{-1} at NaCl concentration of 2000 mg L^{-1} and applied potential of 1.2 V. To investigate the characteristics of adsorption process, many kinetic models including pseudo-frist-order, pseudo-second-order, Weber-Morris, Urano-Tachikawa and S-shape were employed. In addition, adsorption equilibrium data were fitted with isotherm models of Langmuir, Freundlich, Toth and Sips equations. Among them, S-shape kinetic model and Sips isotherm described well the experimental kinetic and equilibrium data, respectively. Compared to the commercial porous carbon (CEP21KS), the porous biocarbons from giant *Miscanthus* prepared in this work showed higher salt adsorption capacity and excellent electrochemical performance because of the high specific surface area and the well-developed pore structures. The theoretical and experimental results of capacitive deionization obtained from this work will be applied to analyze the hybrid processes of capacitive deionization with solar energy, reverse osmosis membrane, microfiltration, microbial fuel cell and photocatalyst.

Chapter 1. Introduction

1.1. Desalination techniques

Population growth, industrialization, environmental pollution and climate change have aggravated a water shortage problem that has become one of the most severe global challenges now [1-4]. Demand of fresh water has increased however available water resources are limited. Because of this, amount of available water per each person has been decreased and water pollution has been accelerated. In addition to lack of water resources, wrong management of these resources has an effect on the availability of water resources. Poor water quality is influenced by presence of any substance or agent that make the water unacceptable or humans hazardous potentially [1]. To relieve this problem, there are some desalination techniques such as electrodialysis, multistage flash, reverse osmosis and capacitive deionization (CDI). Table 1.1 shows advantages and disadvantages of typical desalination techniques. However, these conventional methods have drawbacks including high energy use, secondary pollution, poor efficiency and high cost [3]. On the other hand, capacitive deionization (CDI) possesses advantages such as low energy consumption, environment friendliness, convenient operation and simple equipment structure. Additionally, CDI has emerged as a promising alternative for removal of undesired ion species from various water sources [2-4].

Table 1.1. Advantages and disadvantages of typical desalination techniques.

Techniques	Advantages	Disadvantages	Types
Distillation	▪ High quality of water production ▪ Treatment of feed water with high concentration and large amount	▪ High energy consumption ▪ Corrosion problem of equipment	▪ Multi-stage flash distillation (MSF) ▪ Multiple-effect distillation (MED) ▪ Vapor compression distillation (VCD) ▪ Solar still distillation (SSD)
Reverse osmosis (RO)	▪ Non chemical change of substance ▪ Separation of specific substance possible ▪ Compact system ▪ Lower energy consumption than distillation	▪ Being influenced by temperature and pH of feed water ▪ Need to treat concentrated water ▪ Membrane fouling ▪ Relatively low water quality	
Electrodialysis	▪ Eco-friendly process without by-product ▪ Non addition of chemical reagents ▪ Low maintenance cost ▪ Facile pretreatment	▪ Suitability for small scale ▪ Poor efficiency at high concentration	
Capacitive deionization (CDI)	▪ Low energy consumption ▪ Operation possible at room temperature ▪ Superior energy efficiency ▪ Simple equipment composition and maintenance ▪ Facile electrode regeneration	▪ Hard to treat feed water with high concentration	▪ Flow-by CDI ▪ Membrane CDI ▪ Inverted CDI ▪ Flow-electrode CDI ▪ Hybrid CDI

1.2. Capacitive deionization (CDI)

CDI is operated by electrostatic interaction of ions in the electric double layer (EDL) of symmetric porous carbon electrodes at an applied potential [2,5]. The ions in feed water is adsorbed on the surface of electrodes and fresh water is flowed into outlet when the potential is applied. When the potential is removed or opposite potential is applied, adsorbed ions by electrostatic interaction are desorbed into a concentrated stream (Figure 1.1). CDI is usually operated under 1.23 V to avoid water electrolysis.

Figure 1.2 shows the timeline of scientific development in CDI field. Studies for CDI have been conducted since the late 1960s, when it was called "electrochemical demineralization". The followed four decades saw only intermittent advances to this technology [6]. Over the last two decades, however, an explosion in the academic interest in CDI technology has occurred with various CDI cell architectures constantly springing up, leading to tremendous advances in the CDI field.

CDI-based technologies has been used in various applications of water desalination [7], water purification [8], resource recovery [9], water disinfection [10], synergistic combination with other technologies [11], energy harvesting [12] and CO_2 capture [13].

1.2.1. Types of CDI

The most conventional CDI called flow-by CDI is made up of symmetry porous carbon electrodes allowing capacitive ion adsorption and a separator between electrodes to avoid short circuit [14]. Figure 1.3 shows typical CDI cell architectures. CDI cells can be largely divided into two types (i.e., non-Faradaic or Faradaic CDI). Flow-by CDI, flow-through CDI, MCDI, ICDI and FCDI remove ions using non-Faradaic process including electrostatic and capacitive effects. On the other hand, HCDI, desalination battery and CID are operated by Faradaic process that is a reversible redox reaction [4].

Electrosorption

Current collector (-)

e⁻

Current collector (+)

Water flow

Desorption

Current collector (+)

Current collector (-)

e⁻

Water flow

Cation

Anion
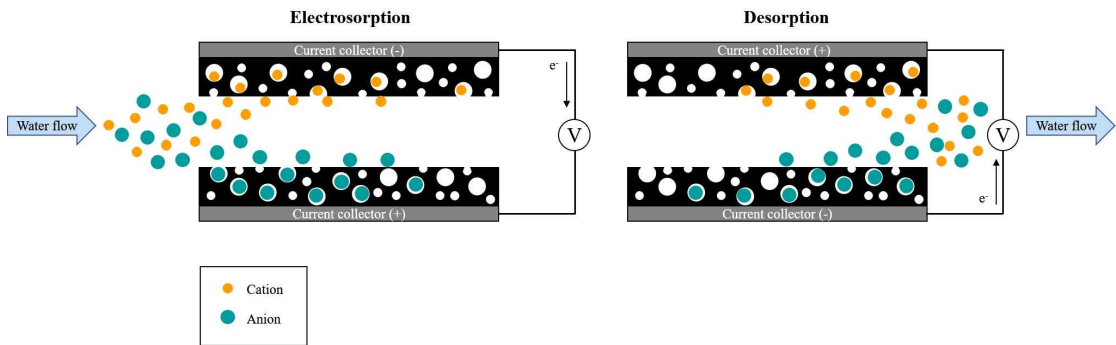
Figure 1.1. Schematic illustration of CDI system.
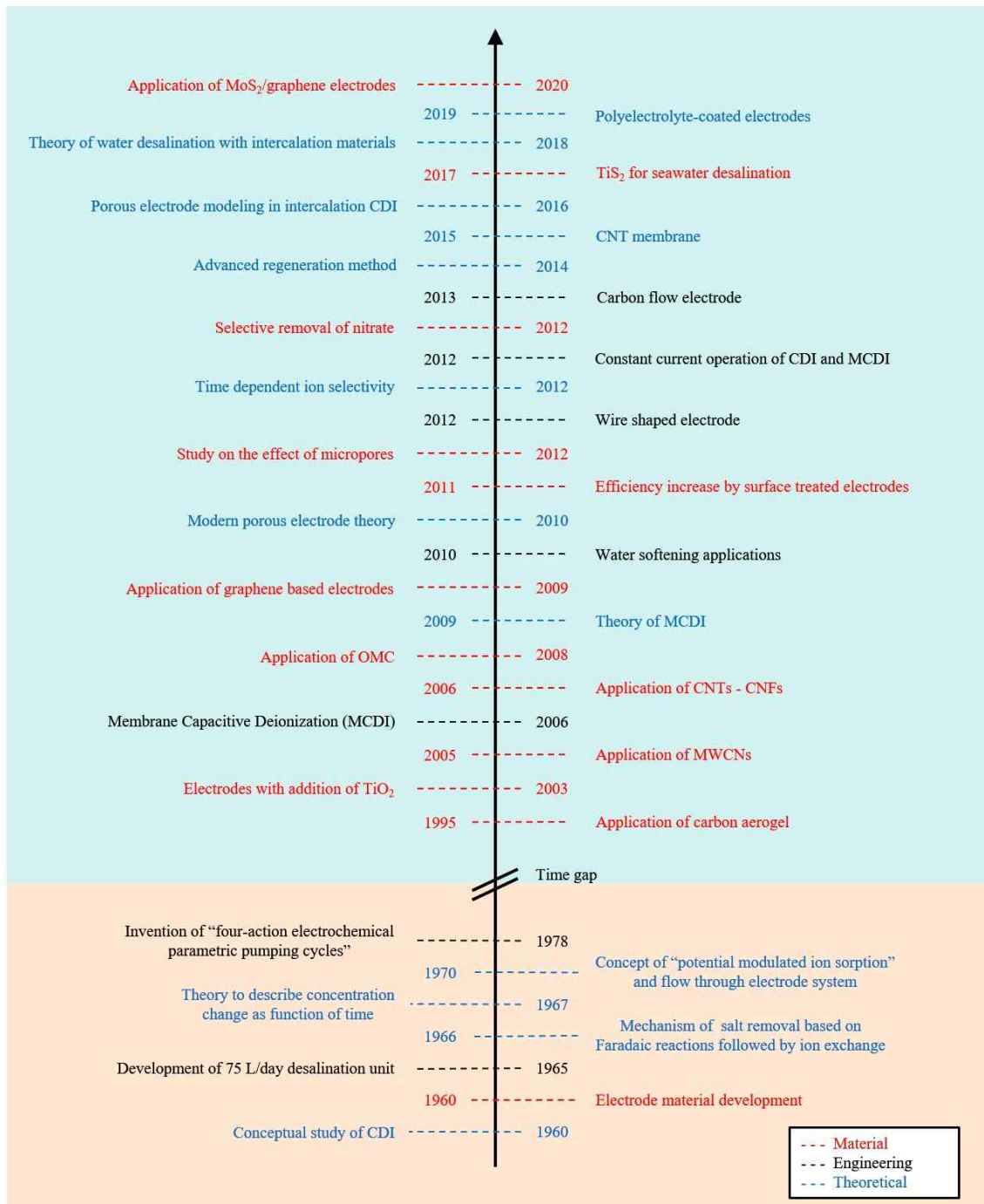
Figure 1.2. Timeline of scientific developments of CDI (modified from [6]).
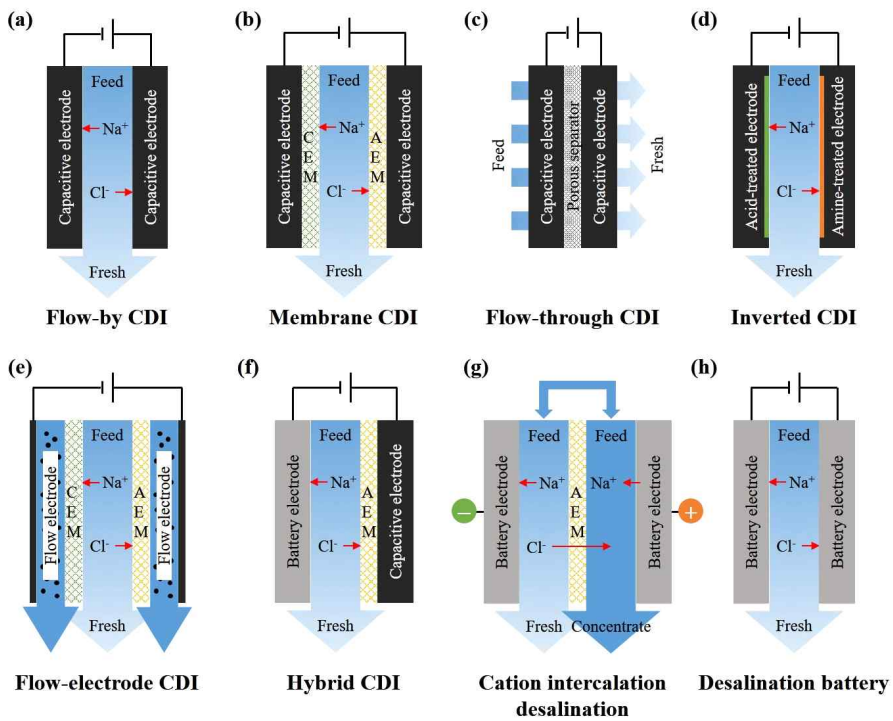
Figure 1.3. Typical cell architectures of various CDI: (a) Flow-by CDI, (b) Membrane CDI, (c) Flow-through CDI, (d) inverted CDI, (e) Flow-electrode CDI, (f) Hybrid CDI, (g) Cation intercalation desalination, and (h) Desalination battery (adapted from [4]).

1.2.2. Carbon materials for CDI electrode

It has been known that electrode materials play an important role in the operation of CDI devices [15,16]. In general, large specific surface area, uniform and small particle size, proper pore size distribution and excellent electrical conductivity are required for ideal electrode materials [17] including activated carbon [18,19], carbon nanotubes [20], carbon fibers [21,22], carbon aerogels [23,24], heteroatom doping carbon [25-28] and graphene [29-33] and biocarbons [34,35]. Among them, carbon materials derived from biomass have received attention because it is environmental friendly, low-cost and abundant resources.

1.2.3. Biomass derived carbons

Biomass derived carbons are used in widespread applications of contaminants adsorption [36], sensors [37], electrochemical energy storage [38], fuel cells and hydrogen storage [39-41]. Table 1.2 shows many previous researches using the biomass derived carbons for the CDI application. Porous biocarbons usually can be obtained by carbonization under the inert gas atmosphere. Additionally, activation process is added to increase specific surface area and develop pore structures. Activation process can be divided into physical and chemical activation. As shown in Figure 1.4, chemical activation is conducted at relatively low in one step or two steps, while physical activation is carried out at comparatively higher temperature than chemical activation in two steps. As shown in Table 1.3, each method has advantages and disadvantages. Th physical activation including steam, CO_2 and air is eco-friendly and simple, but requires high activation temperature in other words lots of energy is consumed. On the other hand, chemical activation such as KOH, H_3PO_4, $ZnCl_2$ is effective to develop pore structures and can be conducted in one step, but washing process is required after activation to remove chemical residues. Among them, $ZnCl_2$ activation is simple and efficient to produce porous carbons and limits the formation of tar. In addition, Liu et al. [42] reported that the presence of a small amount of Zn elements and the variation of

oxygen and nitrogen functional groups on surface of the carbon material after $ZnCl_2$ activation increased surface hydrophilicity, which has an advantage as the electrode for CDI application.

Table 1.2. Previous researches for CDI using biomass derived carbon electrodes.

Precursor	Activator	S_{BET} $(m^2\ g^{-1})$	Concentration of feed water	Applied potential (V)	Salt adsorption capacity $(mg\ g^{-1})$	Ref.
Xylose	KHCO$_3$	408	1000 ppm NaCl	1.2	16.29	[3]
Chitosan	KOH	2334	1000 ppm KCl	1.2	26.6	[43]
			1360 ppm KNO$_3$		35.3	
			2350 ppm K$_2$SO$_4$		68.2	
Tamarind shell	Urea and KOH	410	600 ppm NaCl	1.2	18.8	[44]
Date seed	KOH	1021	250 ppm NaCl	1.2	22.2	[45]
Pinecone	H$_3$PO$_4$	1176	1000 ppm NaCl	1.2	14.62	[46]
Citrus peel	ZnCl$_2$	322	500 ppm NaCl	1.5	10.79	[47]
	KOH	266			8.58	
	H$_3$PO$_4$	25.7			5.22	
Soybean shell	KHCO$_3$	1036	40 ppm NaCl	1.2	16.0	[25]
Almond shell	CO$_2$	450	500 ppm NaCl	1.2	19.2	[48]
Date palm leaflet	KOH	604	100 ppm NaCl	1.8	5.38	[49]
Sugarcane bagasse	KOH and CO$_2$	764	10 mM NaCl	1.2	11.4	[50]
Pine pollen	-	1016	260 ppm NaCl	2.0	19.43	[51]

Physical activation

Inert atmosphere
500 – 800 ℃

Carbonization → Carbon → Gasification

Steam, CO_2 : 750 – 900 ℃
O_2 : 350 – 500 ℃

Biomass precursor

Porous carbon material

Chemical activation

Impregnation → Thermal treatment → Washing

H_3PO_4, $FeCl_3$, $ZnCl_2$

KOH, NaOH

Carbonization → Carbon

Inert atmosphere
500 – 800 ℃

Inert atmosphere
H_3PO_4, $ZnCl_2$: 400 – 600 ℃
$FeCl_3$: 500 – 800 ℃
KOH, NaOH : 800 – 1000 ℃
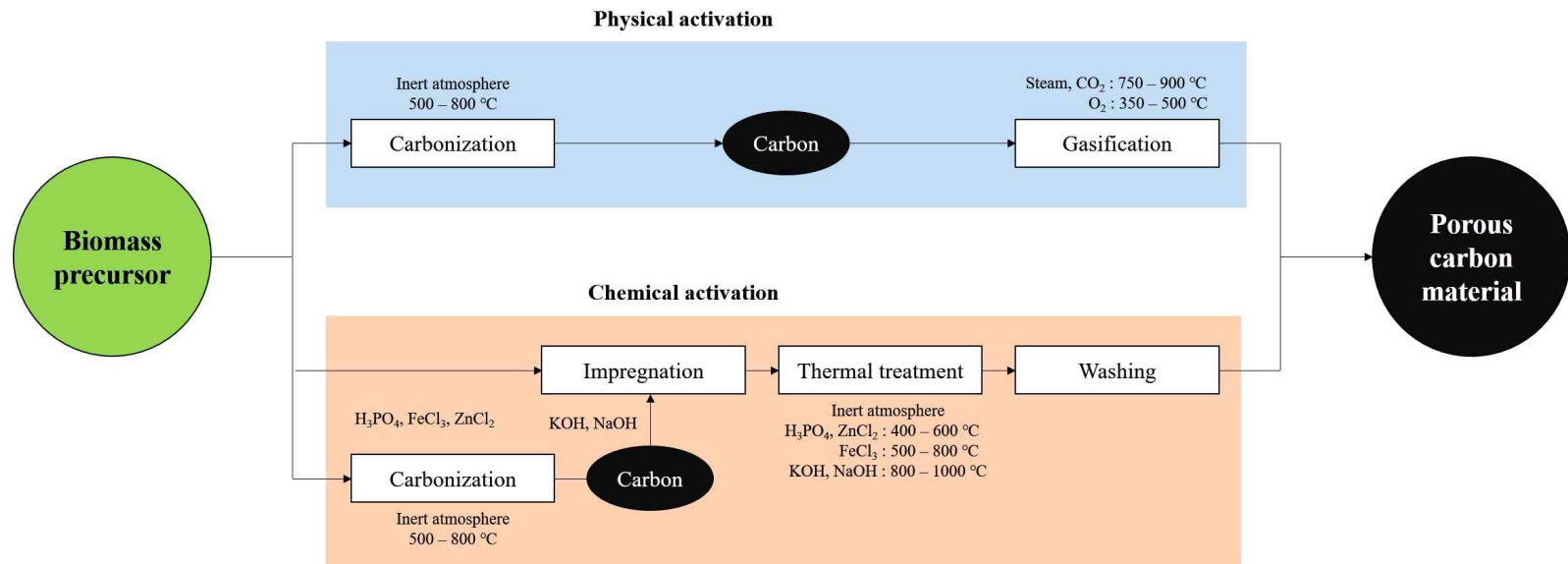
Figure 1.4. Synthesis of porous carbons from biomass (modified from [52]).

Table 1.3. Characteristics of physical and chemical activations.

Activation	Activator	Advantages	Disadvantages
Physical activation	Steam	✓ Simple process and low operation difficulty ✓ Environment-friendly	✓ Requirement of a large amount of heat (> 750 °C)
	CO_2	✓ Environment-friendly and easy handling	✓ Higher reaction temperature of 850 – 1100 °C
	Air	✓ Low cost	✓ Excessive combustion of the raw materials ✓ Fail to effectively form pores
Chemical activation	KOH	✓ High specific surface area and developed micropores ✓ Formation of tar can be effectively suppressed.	✓ Need for neutralization process after activation
	H_3PO_4	✓ Great advantages than $ZnCl_2$ activation in terms of cost	✓ Need for washing after activation to remove an acidic residue ✓ Difficult handling because of using strong acid
	$ZnCl_2$	✓ Simple process and efficiency ✓ The dehydrogenation of $ZnCl_2$ limits the formation of tar ✓ Improvement of hydrophilicity of carbon materials	✓ Need to remove residual zinc and chloride ions

1.3. Research objective

Giant *Miscanthus* has been cultivated to use as energy crop and tourism resources. However giant *Miscanthus* is being neglected because produced bio-ethanol is uneconomic, and giant *Miscanthus* looks unattractive. To use as a carbon material for the CDI electrode, giant *Miscanthus* was carbonized and activated with $ZnCl_2$ simultaneously and finally porous biocarbons were prepared successfully. Control of specific surface area and pore size distribution are important for high-performance CDI. Many researchers have studied about biocarbons. However many studies only focused on increase of the specific surface area. In this work, besides high specific surface area, proper pore size distribution was considered to adsorb ions as fast as and as much as possible. To optimize these characteristics, $ZnCl_2$/GM ratio and activation temperature were controlled. Figure 1.5 shows the overall scope in this study.
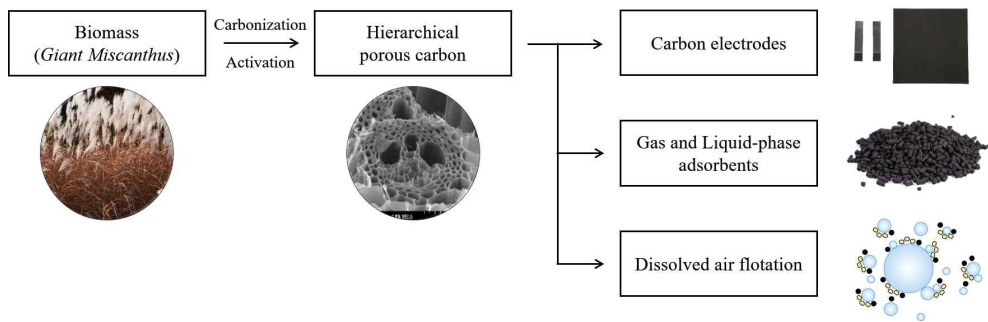
Figure 1.5. Design, synthesis and applications of porous biocarbons.

Chapter 2. Theories and Modeling

2.1. Cottrell equation

Potential step method is measurement of current or charge over the time, which is called as chronoamperometry or chronocoulometry, respectively. This method assumes that mass transfer is only affected by linear diffusion on the electrode. Figure 2.1 illustrates the typical electric double layer that consist of the stern layer and diffusion layer. If the electrochemical reaction is reversible (nernstian), current is only determined by diffusion. Thus, this current is called as diffusion current (i_d) (i.e., Cottrell equation).

$$Rate = \frac{i_d}{nFA} = D_O \frac{dc_O(x,t)}{dx}\Big|_{x=0} \tag{Eq. 2-1}$$

$$i_d = \frac{nFAD_O^{1/2}c_O^*}{\sqrt{\pi t}} \tag{Eq. 2-2}$$

Double layer charging current flows faster than diffusion current because the potential is changed to a step shape in chronoamperometry. Therefore total current is the sum of the diffusion current (Faradaic current) and charging current (non-Faradaic current). Charge (Q) is the integration of diffusion current during the potential step (Eq. 2-3), which is called as chronocoulometry. A diffusion coefficient (D_O) can be calculated from the slope of Anson plot (Eq. 2-4).

$$Q = \int_0^t i_d\, dt = \frac{2nFAD_O^{1/2}c_O^*}{\sqrt{\pi}} t^{1/2} \tag{Eq. 2-3}$$

$$\frac{2nFAD_O^{1/2}c_O^*}{\sqrt{\pi}} \tag{Eq. 2-4}$$
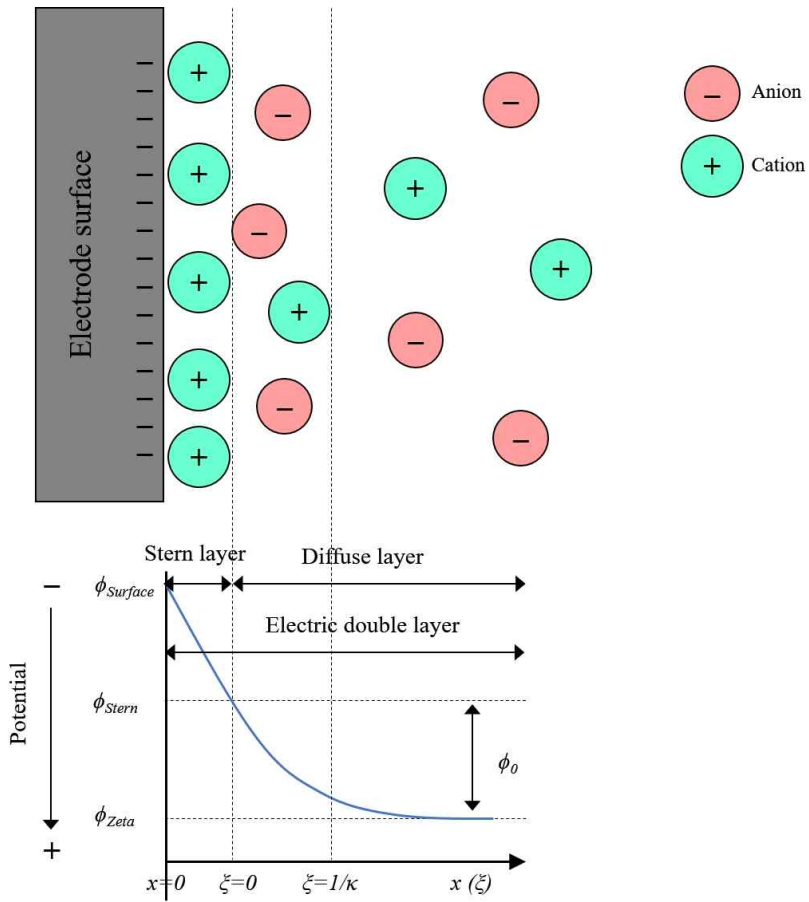
Figure 2.1. Description of the electric double layer.

The value of Q is the summation of integrating both Faradaic current (i_f) and charging current (i_c).

$$Q = \int_0^t i_f \, dt + \int_0^t i_c \, dt = \frac{2nFAD_O^{1/2}c_O^*}{\sqrt{\pi}} t^{1/2} + Q_{dl} \qquad \text{(Eq. 2-5)}$$

If the portion of O is adsorbed on the electrode, total Q is expressed as Eq. 2-6. To measure the amount of adsorbed O (Γ_O, mol cm^{-2}), the value of Q_{ad} is calculated from the intercept gap of the Anson plot with presence or absence of O (Figure 2.2).

$$Q = Q_f + Q_{ad} + Q_{dl} \qquad \text{(Eq. 2-6)}$$
$$Q_{ad} = nFA\Gamma_O \qquad \text{(Eq. 2-7)}$$
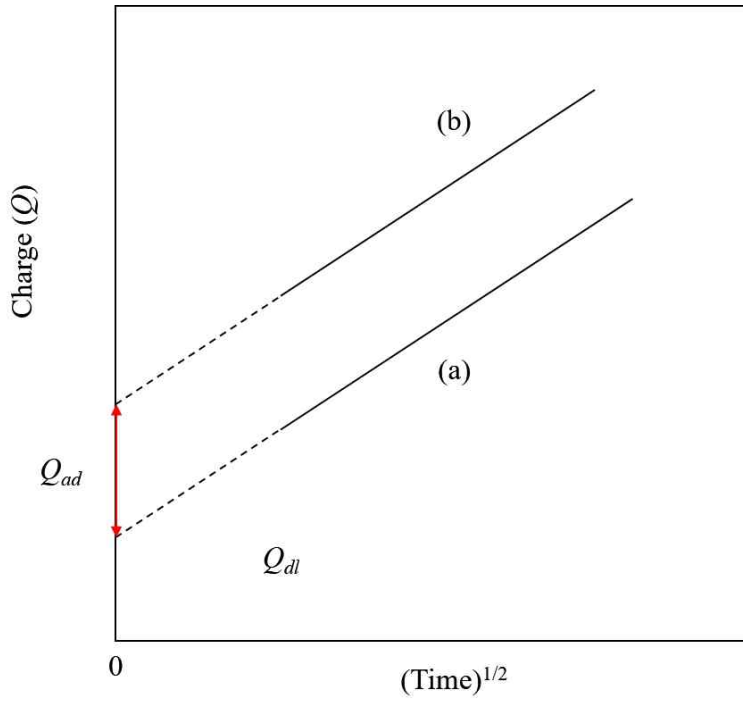
Figure 2.2. Measurement of Q_{dl} and Q_{ad} from the Anson plot.

Mass transfer on the electrode is described as Fick's second law.

$$\frac{\partial c_O(x,t)}{\partial t} = D_O \frac{\partial c_O(x,t)}{\partial x^2} \qquad \text{(Eq. 2-8)}$$

This equation is the partial differential equation, which is difficult to solve analytically. For this, Laplace transformation is used to obtain the solution of partial differential equation.

The initial, semi-infinite and surface boundary conditions are defined as Eq. 2-9, Eq. 2-10 and Eq. 2-11, respectively.

$$c_O(x,0) = c_O^* \qquad \text{(Eq. 2-9)}$$

$$\lim_{x \to \infty} c_O(x,t) = c_O^* \qquad \text{(Eq. 2-10)}$$

$$c_O(0,t) = 0 \,(\text{f or } t > 0) \qquad \text{(Eq. 2-11)}$$

As shown in Figure 2.3, Eq. 2-12 is a converted form from Fick's second law by Laplace transformation. Eq. 2-13 is the solution of ordinary differential equation considering semi-infinite and surface boundary conditions. Finally, the solution of Fick's second law (Eq. 2-14) is obtained as the error function from the solution of ordinary differential equation via inverse Laplace transformation. Figure 2.4 shows the concentration distribution of O using the final solution (i.e., Eq. 2-14) when D_O is 10^{-5} cm^2 s^{-1}.

$$\frac{\partial c_O(x,t)}{\partial t} = D_O \frac{\partial^2 c_O(x,t)}{\partial x^2}$$ ------ (Eq. 2-8)

$$\frac{d^2 \overline{C}_O(x,s)}{dx^2} - \frac{s}{D_O} \overline{C}_O(x,s) = -\frac{c_O^*}{D_O}$$ ------ (Eq. 2-12)

Laplace transformation

Fick's 2nd law (PDE) → ODE

not easy

easy

Solution of PDE ← Solution of ODE

Inverse Laplace transformation

$$\frac{c_O(x,t)}{c_O^*} = erf\left[\frac{x}{2(D_O t)^{1/2}}\right]$$ ------ (Eq. 2-14)

$$\overline{C}_O(x,s) = \frac{c_O^*}{s} - \frac{c_O^*}{s} e^{-\sqrt{s/D_O}\, x}$$ ------ (Eq. 2-13)
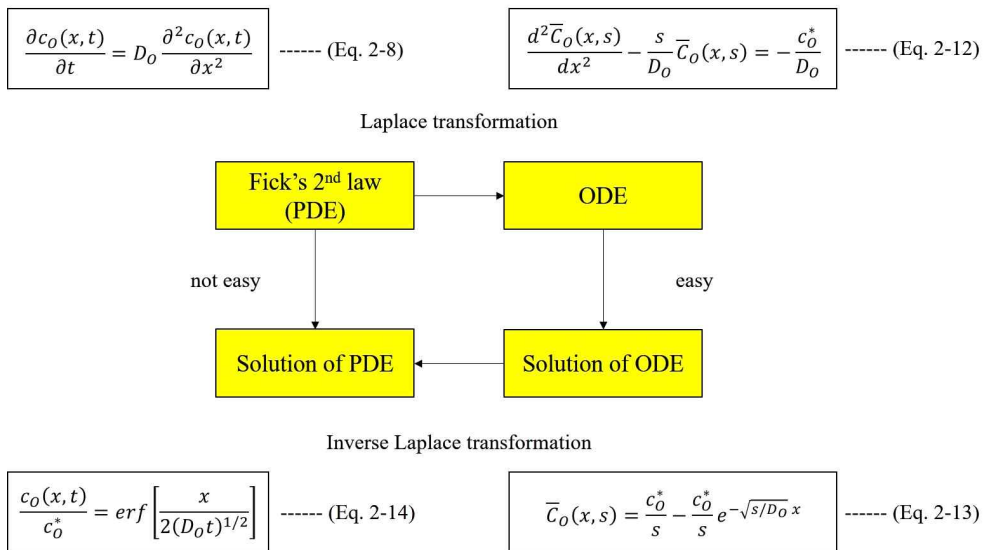
Figure 2.3. Analytic solution of Fick's 2nd law by Laplace transformation.
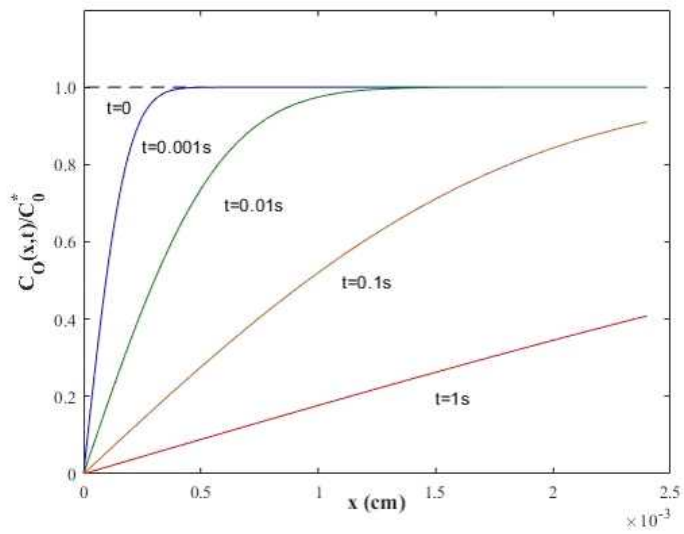
Figure 2.4. Concentration distribution of O in the potential step experiment.

Current is defined as Eq. 2-15 and converted to Eq. 2-16 by Laplace transformation.

$$-J_O(0,t) = \frac{i(t)}{nFA} = D_O \left[\frac{dc_O(x,t)}{dt} \right]_{x=0} \tag{Eq. 2-15}$$

$$\frac{\overline{Id}(s)}{nFA} = D_O \left[\frac{d\overline{C}_O(x,s)}{dx} \right]_{x=0} \tag{Eq. 2-16}$$

Eq. 2-17 is obtained by inserting Eq. 2-13 into Eq. 2-16 when $x = 0$. Cottrell equation (Eq. 2-18) is obtained by inverse Laplace transformation.

$$\overline{I}(s) = \frac{nFAD_O^{1/2}c_O^*}{\sqrt{s}} \tag{Eq. 2-17}$$

$$i(t) = i_d(t) = \frac{nFAD_O^{1/2}c_O^*}{\sqrt{\pi t}} \tag{Eq. 2-18}$$

2.2. Adsorption kinetics

The adsorption of adsorbate on the adsorbent is carried out by diffusion or mass transfer process based on the three steps as follows:

Step 1. External diffusion

    Mass transfer from the boundary liquid film to the surface of the solid.

Step 2. Internal diffusion

    Mass transfer from the surface to the intra-particle active sites.

Step 3. Adsorption

    Uptake of adsorbate by complexation, sorption or intra-particle precipitation

Study of adsorption kinetics provides information about the possible mechanism of adsorption. To evaluate the kinetic experimental data, many kinetic models were used. The pseudo-first-order and pseudo-second-order kinetic models were applied to examine the rate controlling step of biocarbons in the adsorption process. And the intraparticle mass transfer diffusion models such as Weber-Morris and Urano-Tachikawa equations were used to understand the diffusion mechanism of the adsorption system in this work. In addition, the S-shape kinetic model was employed. Various kinetic model equations and parameters are listed in Table 2.1. In Pseudo-first-model, q_e (mg g^{-1}), q_t (mg g^{-1}) and k_1 (s^{-1}) mean amount of adsorbate at equilibrium, amount of adsorbate at time t (s) and the rate constant of the pseudo-first order equation, respectively. The parameter of k_2 (g mg^{-1} s^{-1}) represents a rate constant of the pseudo-second-order equation. The intraparticle diffusion coefficients in the solid, K_i (mg g^{-1} s$^{-0.5}$) and D_i (m^2 s^{-1}) can be calculated from Weber-Morris model and Urano-Tachikawa, respectively. In addition, b (s^{-1}) is the adjustable parameter and n is the rate constant of adsorption/desorption ratio in the S-shape kinetic model. The kinetic parameters were determined by nonlinear regression methods using the software (MATLAB 2021a, MathWorks, USA).

Table 2.1. Description of the various adsorption kinetic models.

Kinetic model	Non-linear form	Description	Ref.
Pseudo-first-order	$q_t = q_e\left(1 - e^{-k_1 t}\right)$	q_e (mg g^{-1}) : amount of adsorbate at equilibrium	[53]
		q_t (mg g^{-1}) : amount of adsorbate at time t (s)	
		k_1 (s^{-1}) : rate constant of the pseudo-first-order equation	
Pseudo-second-order	$q_t = \dfrac{k_2 q_e^2 t}{1 + k_2 q_e t}$	k_2 (g mg^{-1} s^{-1}) : the rate constant of the pseudo-second-order equation	[54,55]
Weber-Morris	$q_t = K_i t^{0.5}$	K_i (mg g^{-1} s$^{-0.5}$) : diffusion coefficient in the solid	[56,57]
Urano-Tachikawa	$q_t = q_e\left(1 - e^{-4\pi^2 D_i t/d_p^2}\right)^{0.5}$	D_i (m^2 s^{-1}) : diffusion coefficient in the solid	[58]
S-shape	$q_t = \dfrac{q_e b t^{1/n}}{1 + b t^{1/n}}$	b (s^{-1}) : adjustable parameter	
		n : rate constant of adsorption/desorption ratio	

2.3. Adsorption isotherms

Adsorption isotherm describes the relationship between the amount of adsorbed ion and the ion concentration remaining in solution [56]. The adsorption isotherm is one of the most important data to understand the mechanism on the adsorption process [59]. There are many equations for analyzing experimental adsorption equilibrium data. The equation parameters of equilibrium models often provide some insight into both the adsorption mechanism and affinity of the adsorbent. In this work, various adsorption isotherms such as Langmuir, Freundlich, Toth and Sips equations were employed to predict adsorption equilibrium behaviors. The isotherm equations and parameters are listed in Table 2.2.

As the ion concentration increases in the Langmuir model, the equilibrium adsorption amount increases while the adsorption sites are not saturated. The adsorption capacity and adsorption affinity can be determined from isotherms. The Freundlich isotherm is an empirical model employed to describe heterogeneous systems [60]. The Toth isotherm is an empirical modified form of the Langmuir model to cut down the error between the experimental and predicted values [61]. This model is most useful in describing heterogeneity of adsorption systems at the both low and high adsorbate concentration [62]. This equation is equal to Langmuir model when $n = 1$. Therefore the parameter n indicates the heterogeneity of the adsorption system [61]. In other words, if n deviates from 1, the adsorption system becomes heterogeneous. Sips isotherm model is a combined form of the Langmuir and Freundlich models [63]. This model is proper for predicting heterogeneous adsorption system, thereby avoiding the limitation of increased adsorbate concentration normally related to the Freundlich model [64]. Therefore this model predicts the Freundlich model at low adsorbate concentration, while it follows the Langmuir model (monolayer adsorption) at high concentration. The parameters of the Sips isotherm model are pH, temperature, and concentration dependent [65,66] and isotherm constants determined by linearization and nonlinear regression differ [67].

Table 2.2. Description of the various adsorption isotherms.

Models	Non-linear form	Description	Ref.
Langmuir	$q_e = \dfrac{q_{m_L} K_L C_e}{1 + K_L C_e}$	C_e (mg L^{-1}) : equilibrium concentration	[53]
		q_e (mg g^{-1}) : equilibrium adsorption capacity	
		q_{m_L} (mg g^{-1}) : maximum adsorption capacity	
		K_L (L mg^{-1}) : constant associated with the adsorption process energy and the affinity of the binding sites	
Freundlich	$q_e = K_F C_e^{1/n_F}$	n_F : constant affecting the adsorption intensity	[60]
		K_F (L mg^{-1}) : constant related to adsorption capacity	
Toth	$q_e = \dfrac{q_{m_T} K_T C_e}{\left[1 + \left(K_T C_e\right)^{n_T}\right]^{1/n_T}}$	q_{m_T} (mg g^{-1}) : maximum adsorption capacity	[61−63]
		n_T : constant related to heterogeneity	
		K_T (L mg^{-1}) : constant related to adsorption affinity	
Sips	$q_e = \dfrac{q_{m_S} K_S C_e^{1/n_S}}{1 + K_S C_e^{1/n_S}}$	q_{m_S} (mg g^{-1}) : maximum adsorption capacity	[64−67]
		n_S : parameter of heterogeneity	
		K_S (L mg^{-1}) : constant related to adsorption capacity	

Chapter 3. Experimental

3.1. Preparation of porous biocarbons

3.1.1. Chemicals

Giant *Miscanthus* (GM) used in this experiment was provided by the Korea Rural Development Administration. Before the experiment, giant *Miscanthus* was thoroughly washed and dried. Afterward it was cut and crushed for 2 min by blender before carbonization. Zinc chloride was selected as the chemical activator in this work and bought from DaeJung Chemicals & Metals. All solutions were prepared using distilled water. All other chemicals were analytical grade and used as received.

3.1.2. Carbonization and activation

150 g of giant *Miscanthus* was mixed with 750 mL of distilled water and 150 g of $ZnCl_2$ with different weight ratios of $ZnCl_2$/GM were 1, 2 and 4. The impregnation was conducted in a shaking incubator for 1 h at 50 ℃ and then 12 h at 25 ℃. The impregnated giant *Miscanthus* was filtered and dried at 80 ℃ for 12 h in vacuum oven. The carbonization and activation were carried out simultaneously in an inert N_2 atmosphere at 600, 700 and 800 ℃ for 1 h with a heating rate of 5 ℃ min^{-1}, and then cooled to room temperature within a furnace in the same N_2 atmosphere (Figure 3.1). The obtained samples were soaked in 1 M HCl for 12 h to remove the zinc compounds, and then they were washed with hot and cold distilled water several times until the neutral pH. The wet samples were dried at 60 ℃ for 12 h in vacuum oven and crushed by ball mill to make powdered porous biocarbons. Figure 3.2 shows flowchart for preparation of the porous biocarbons derived from giant *Miscanthus*.
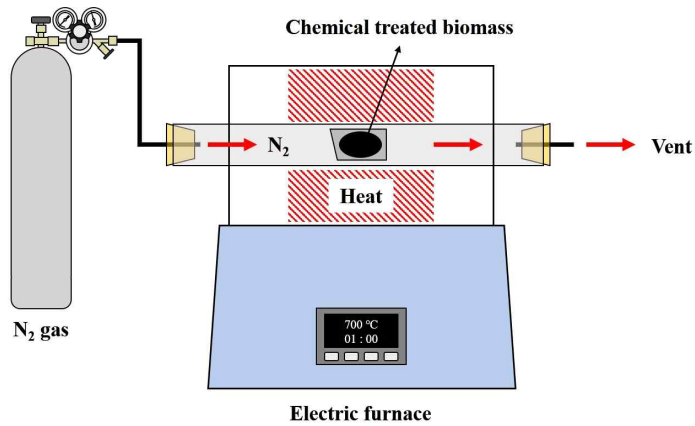
Figure 3.1. Experimental apparatus for carbonization and activation.

Figure 3.2. Flowchart for preparation of the porous biocarbons.

3.2. Characterization of porous biocarbons

To evaluate physical and chemical properties of biocarbons prepared from giant *Miscanthus*, various many instrumental analyses of TGA, SEM, BET, XRD, Raman and FTIR were employed. Thermo gravimetric analysis (TGA) (DTG-60H, Shimadzu, Japan) was carried out to verify major components of the raw giant *Miscanthus*. Giant *Miscanthus* was placed in a pottery crucible and heated from room temperature to 900 °C under N_2 and air atmosphere. A field emission scanning electron microscope (FE-SEM) (S-4800, Hitachi, Japan) was used to observe the surface morphology of biocarbons. N_2 adsorption/desorption measurements were conducted at 77 K to track the specific surface are and pore size distribution of porous biocarbons using a Belsorp mini II (BEL, Japan). Before the measurement, the biocarbons were degassed under vacuum for 6 h at 300 °C. The specific surface area was evaluated by the Brunauer-Emmet-Teller (BET) method at relative pressure (P/P_0) of 0 to 0.45. X-ray diffraction (XRD) (D/MAX Ultima III, Rigaku, Japan) measurement was conducted through nonmonochromatic Cu-Kα X-ray at 40 kV and 40 mA. The structure of the carbon was further characterized using a NRS-5100 (JASCO, Japan) Raman spectroscopy at room temperature with an excitation wavelength of 532 nm from a diode-pumped solid-state laser. The surface functional groups on the biocarbons were analyzed by FT-IR spectra using a IRPrestige-21 (Simadzu, Japan). Prior to the analysis, KBr disks were prepared by mixing biocarbon powders in KBr. The spectra were recorded in the range of $4000 - 400$ cm^{-1}.

3.3. Electrochemical measurement

3.3.1. Preparation of electrodes

The giant *Miscanthus* derived carbons (GMCs) were mixed with 10% styrene butadiene rubber, 2% aqueous carboxymethyl cellulose and distilled water. To make homogeneous carbon slurry, they were blended for 1 h in paste mixer. After blending, the slurry was coated with 1 x 1 cm^2 on graphite sheet and dried at 100 ℃ for 4 in the oven slowly gradually increasing the temperature (Figure 3.3).

3.3.2. Electrochemical properties

To estimate the electrochemical properties of carbon samples, cyclic voltammetry (CV), chronoamperometry (CA) and electrical impedance spectroscopy (EIS) were conducted in three electrode system of electrochemical workstation (CHI 660E, CH Instruments, USA) in NaCl electrolyte solution. The platinum wire and the saturated calomel electrode were employed as the counter electrode and the reference electrode, respectively. The CV was performed in the range of –0.5 to 0.5 V and scan rate of 5 to 100 mV s^{-1}. The specific capacitance was determined from the CV curves from the following relationship:

$$C_{CV} = \frac{A}{\Delta V \times v \times m} \qquad \text{(Eq. 3.1)}$$

, where A is the integral area of the cyclic voltammogram loop (A V), ΔV is the sweep potential window (V), v is the scan rate (V s^{-1}) and m is the mass of the electrode materials at each electrode (g). The CA were conducted at 0 to 0.15 V for 3 min to evaluate a diffusion coefficient of electrolyte ions. The EIS were performed in the frequency range of 0.1 Hz - 100 kHz at an open circuit potential with an ac perturbation of 5 mV.
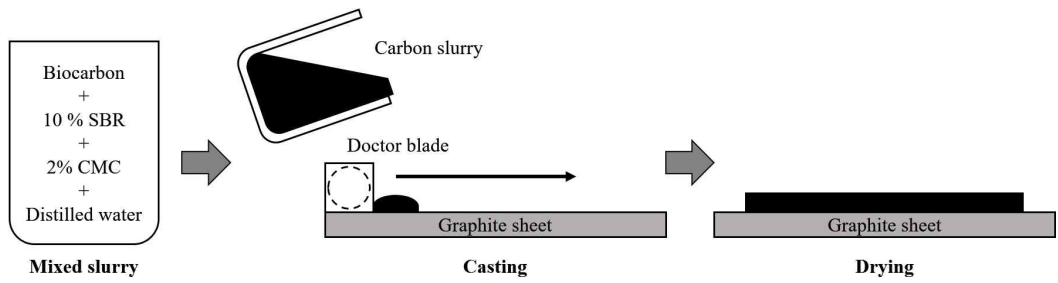
Figure 3.3. Preparation of the porous biocarbon electrodes.

3.4. Performance of CDI

To evaluate CDI performance, the unit cell was assembled and the CDI experiment was carried out. 16 x 16 cm^2 of two acrylic plates were prepared and one of them had three holes with 1 cm of diameter to allow the saline water to flow from both diagonal ends to the center. Two carbon electrodes were cut into 9.5 x 9.5 cm^2 and one of them had a hole at the center. Anion exchange membrane (AEM, Fujifilm type II) and cation exchange membrane (CEM, Fujifilm type II) were used and cut to the same size as electrodes. The MCDI unit cell was constructed by staking ion exchange membranes on the carbon electrodes face to face and nylon spacer was inserted between ion exchange membranes (Figure 3.4). As shown in Figure 3.5, CDI apparatus was prepared to evaluate CDI performance of each carbon electrode. Feed solution was provided with a constant flow rate and operation potential was applied constantly to experiment on adsorption/desorption of NaCl. To observe the change of NaCl concentration, a conductivity meter was set up at the vent. Different operation conditions of the flow rate, applied potential and NaCl concentration were controlled to estimate adsorption/desorption properties in CDI process. First, to understand an effect by the flow rate (15 – 30 mL min^{-1}), adsorption and desorption were performed for 3 min at 1.2 V. Second, different applied potentials (0.6 – 1.2 V) were considered at the optimum flow rate of 15 mL min^{-1} of and NaCl concentration of 100 mg L^{-1}. Third, different concentrations of NaCl (100 – 2000 mg L^{-1}) were applied at 15 mL min^{-1} and 1.2 V. The obtained CDI data were used to understand adsorption kinetic and isotherm behaviors.
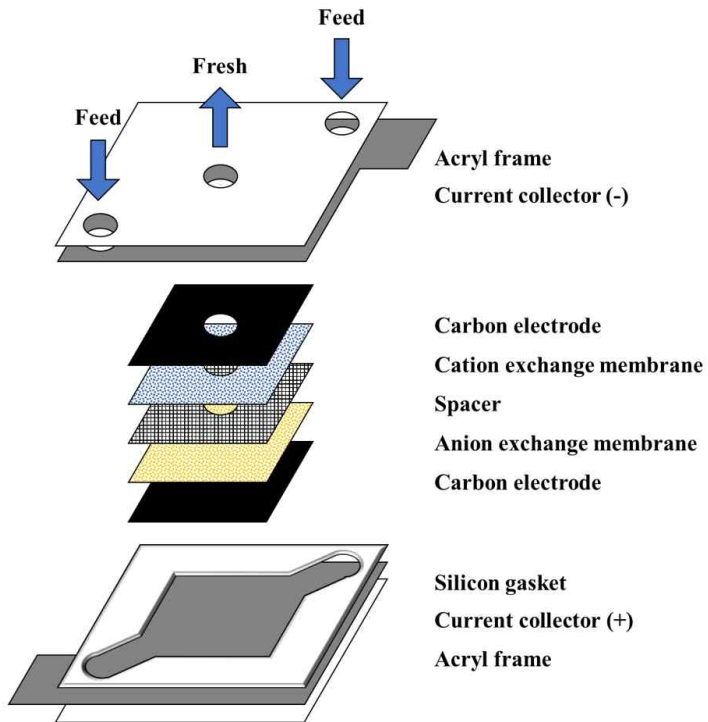
Figure 3.4. Schematic diagram of the MCDI cell structure.
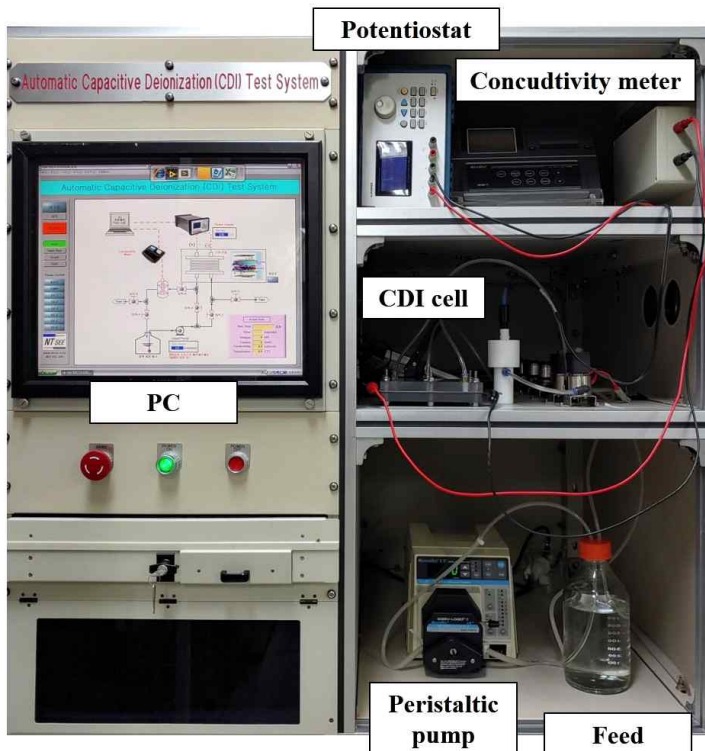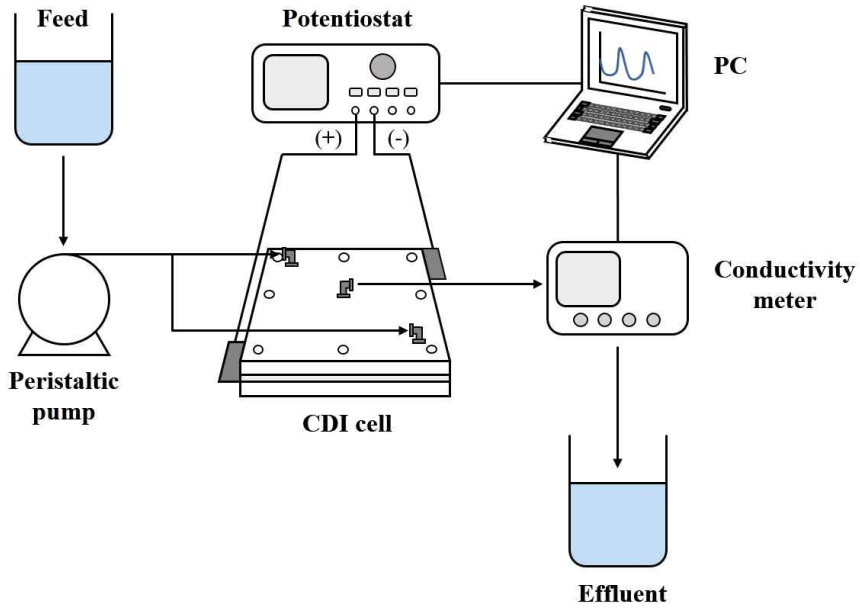
Figure 3.5. Experimental apparatus and process of CDI.

Chapter 4. Results and Discussion

4.1. Characterization

4.1.1. Thermogravimetric analysis (TGA)

TGA is a thermal decomposition analysis which measures the mass change of samples with temperatures. Physical and chemical properties can be obtained from TGA. To estimate the suitability for carbon materials, thermogravimetric analysis of the raw giant *Miscanthus* was conducted. Many factors including the applied temperature and compositions of biomass determine the final physical and chemical properties. Figure 4.1 shows the TGA curves for giant *Miscanthus* composing of lignocellulosic materials of cellulose, hemicellulose, and lignin under air and inert N_2 conditions at a heating rate of 10 ℃/min. According this figure, thermal degradation under N_2 condition takes place in three main steps. The first weight loss began at 40 ℃ and gradually increased up to 250 ℃. In the second step, there is a sudden and sharp weight loss from 250 to 350 ℃ under both air and N_2 gas atmosphere, which means the decomposition of hemicellulose and cellulose [68]. In third step, slow weight loss corresponding to the slow degradation of lignin can be observed under inert N_2 condition unlike air condition. The final yields of giant *Miscanthus* at 900 ℃ under air and N_2 were 1.3 % and 13.3 %, respectively.
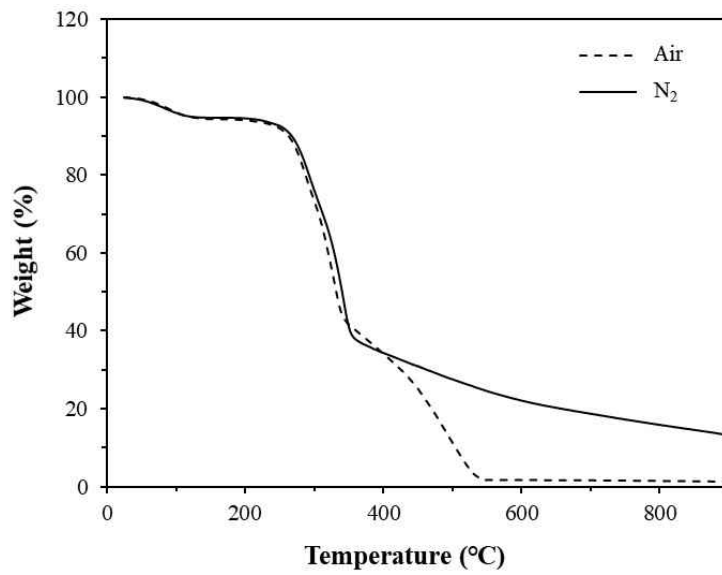
Figure 4.1. TGA results of giant *Miscanthus* under air and N_2 conditions.

4.1.2. Field emission scanning electron microscopy (FE-SEM)

To evaluate the morphological and structural properties, FE-SEM images were obtained for various samples with and without $ZnCl_2$ impregnation. Figure 4.2 illustrates examples of scanning electron micrographs for the prepared GMCs depending on the $ZnCl_2$ impregnation ratio at different magnifications. GMC samples had some aligned open channels, which were probably derived from the plant cell structures present in giant *Miscanthus* before activation. The FE-SEM image of the GMC700-0 at the higher magnification showed a smooth surface as observed in Figure 4.2(a2). On the other hand, GMC700-1, GMC700-2 and GMC700-4 possess these open channels and some opening up of the micron-sized spots generated during $ZnCl_2$ activation (Figure 4.2(b-d)). It was found from the SEM results that $ZnCl_2$ develops defects and pore structures in the vicinity of the carbon surface. Thus, the formation of more internal pores of smaller diameter acts as possible adsorption sites.
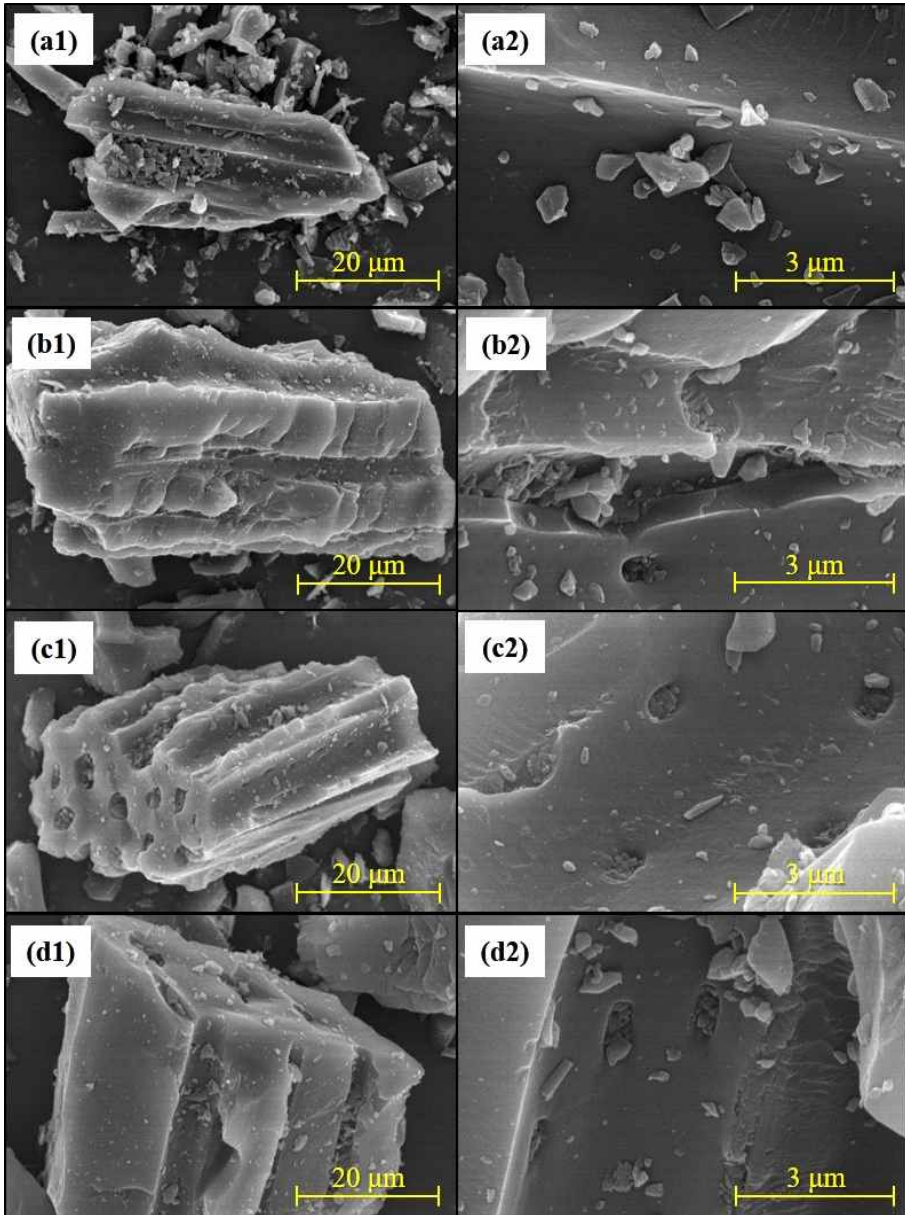
Figure 4.2. FE-SEM images of (a) GMC700-0, (b) GMC700-1, (c) GMC700-2, (d) GMC700-4 (a1, b1, c1, d1: images at low magnification and a2, b2, c2, d2: images at high magnification).

4.1.3. BET analysis

Generally specific surface area and pore size distribution are key factors of porous adsorbents. N_2 adsorption/desorption isotherm data were measured at 77 K to determine the specific surface area and pore size distribution of the pristine and $ZnCl_2$ activated GMCs. As shown in Figure 4.3, the adsorption/desorption isotherms of GMCs typically increased in the relative pressure range of $0 - 0.4$. These results are attributed to microporous activated carbon. According to the International Union of Pure and Applied Chemistry (IU-PAC) classification, the adsorption curves of all GMCs were typical type I isotherms and did not exhibit hysteresis loops as shown in Figure 4.5. In general, Type I isotherms are shown in the microporous solids with relatively small external surfaces such as activated carbons, molecular sieve zeolites and certain porous oxides [69]. On the other hand, GMC700-0 without $ZnCl_2$ activation showed a relatively low amount of N_2 adsorption/desorption and remained steady throughout the entire relative pressure range, because of low surface area and less pores than $ZnCl_2$ treated GMCs. Table 4.1 summarizes the BET surface area, pore volume and mean pore diameter. The BET surface area of the GMC700-0 was 420 m^2 g^{-1}. It was larger than previous results of petro-based carbons and other wood chars (in the range of $1-10$ m^2 g^{-1}) [70−72]. This result may come from the alined open channels inside the giant *Miscanthus* as shown in FE-SEM images. Besides, BET surface area of the GMCs considerably increased after $ZnCl_2$ activation. The BET surface area of GMCs with $ZnCl_2$ activation are in the range of 994 to 1661 m^2 g^{-1}. Among them, the GMC700-4 prepared at the $ZnCl_2$/GM ratio of 4 and activation temperature of 700 ℃ possessed larger surface area than the commercial carbon (CEP21KS). The total pore volume largely increased to 0.874 mL g^{-1} compared to GMC700-0 (0.189 mL g^{-1}). In addition, peaks of pore size distribution were broaden and shifted to right as the $ZnCl_2$ impregnation ratio increased. The mean pore size of GMC700-4 increased from 1.800 to 2.105 nm after activation, which means that the micropores of GMC700-4 were further converted to mesopores. On the other hand, the effect of activation temperature was insignificant. Contrary to expectation, the surface area was not highly dependent on the temperatures.

(a)

(b)
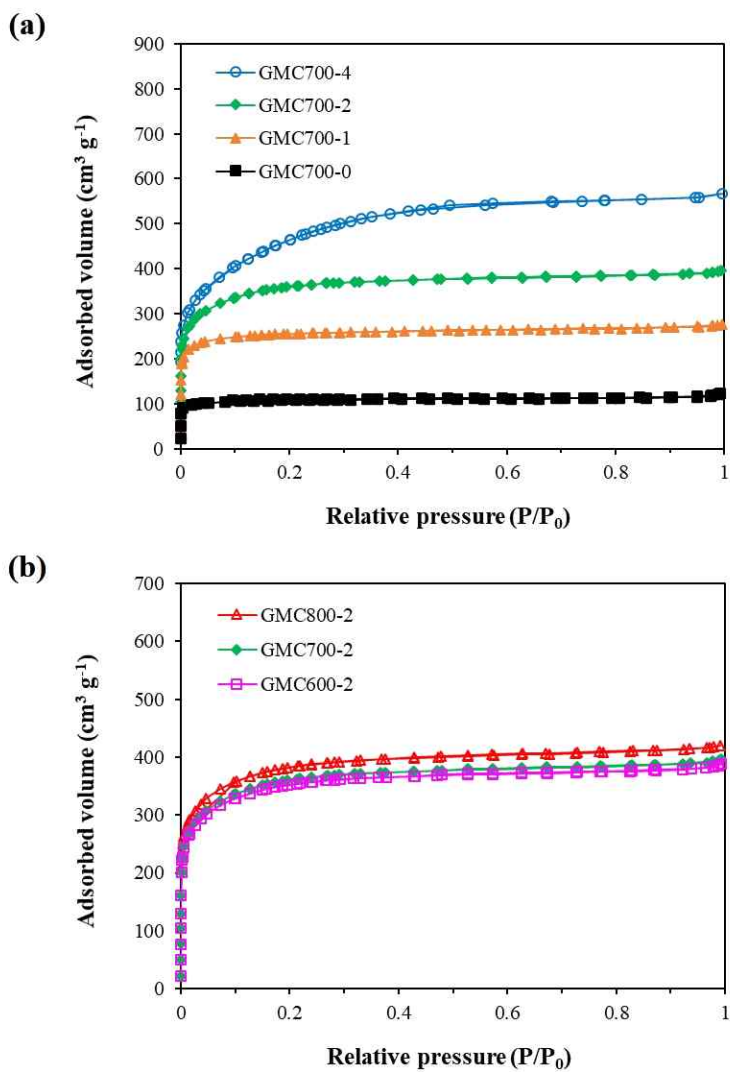
Figure 4.3. N_2 adsorption/desorption isotherms of the GMCs depending on $ZnCl_2$/GM ratio (a) and activation temperatures (b).
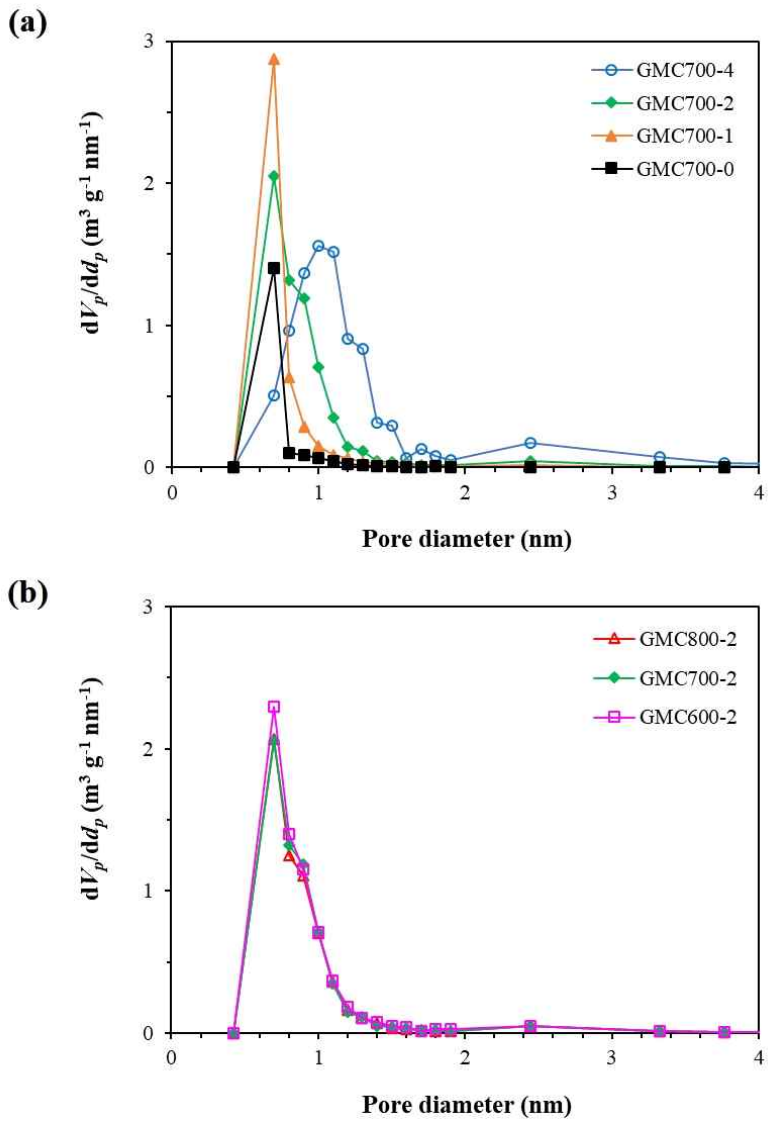
Figure 4.4. Pore size distribution of the GMCs depending on ZnCl$_2$/GM ratio (a) and activation temperatures (b).
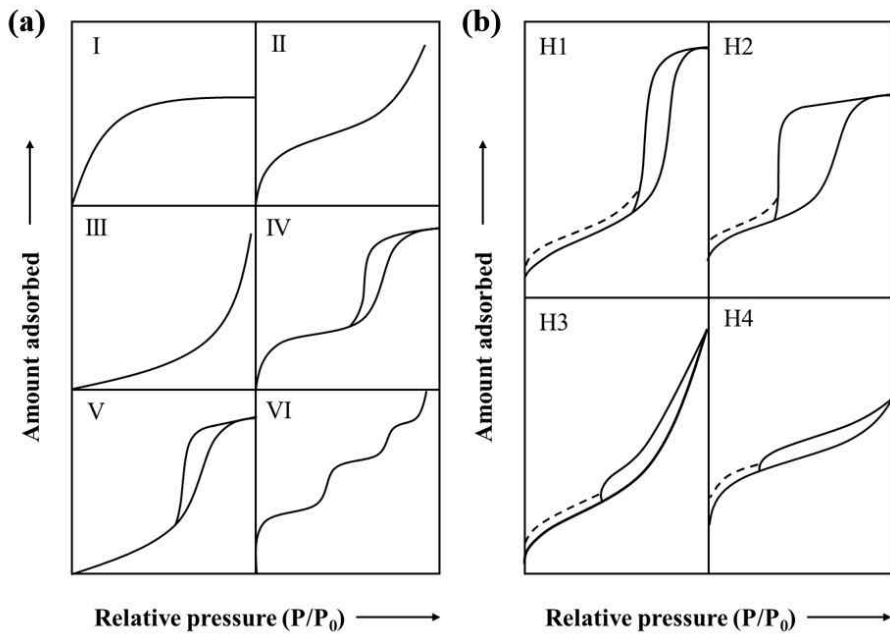
Figure 4.5. Types of physisorption isotherms (a) and hysteresis loops (b) (modified by [69]).

Table 4.1. Surface area, pore volume and pore diameter of the GMCs.

Sample	BET surface area (m^2 g^{-1})	Total pore volume (mL g^{-1})	Mean pore diameter (nm)
CEP21KS	1553	0.699	1.800
GMC700-0	420	0.189	1.803
GMC700-1	994	0.427	1.717
GMC700-2	1338	0.611	1.826
GMC700-4	1661	0.874	2.105
GMC600-2	1304	0.598	1.835
GMC800-2	1428	0.649	1.819

4.1.4. X-Ray diffraction (XRD)

The XRD analysis was conducted to understand the crystalline structure of the carbon layers of GMCs depending on $ZnCl_2$ impregnation ratio and activation temperatures. As shown in Figure 4.6, XRD results of GMCs were followed patterns of amorphous carbon materials. All GMCs had typical two broad peaks appeared at $\sim 26°$ and $\sim 43°$ corresponding to the (002) and (100) planes of the graphitic structure, which is a feature of graphitic carbon materials [73]. It represents that they have disordered structures. The weak (002) peak means low graphitization degree and disordered arrangement of carbon layers. The (100) peak indicates that the presence of honeycomb structure formed by sp^2 hybridized carbons. In addition, there were little differences in peak intensity among GMCs. This result indicates the negligible effects of the introduction of $ZnCl_2$ during pyrolysis and activation temperature on the crystalline structure of GMCs.
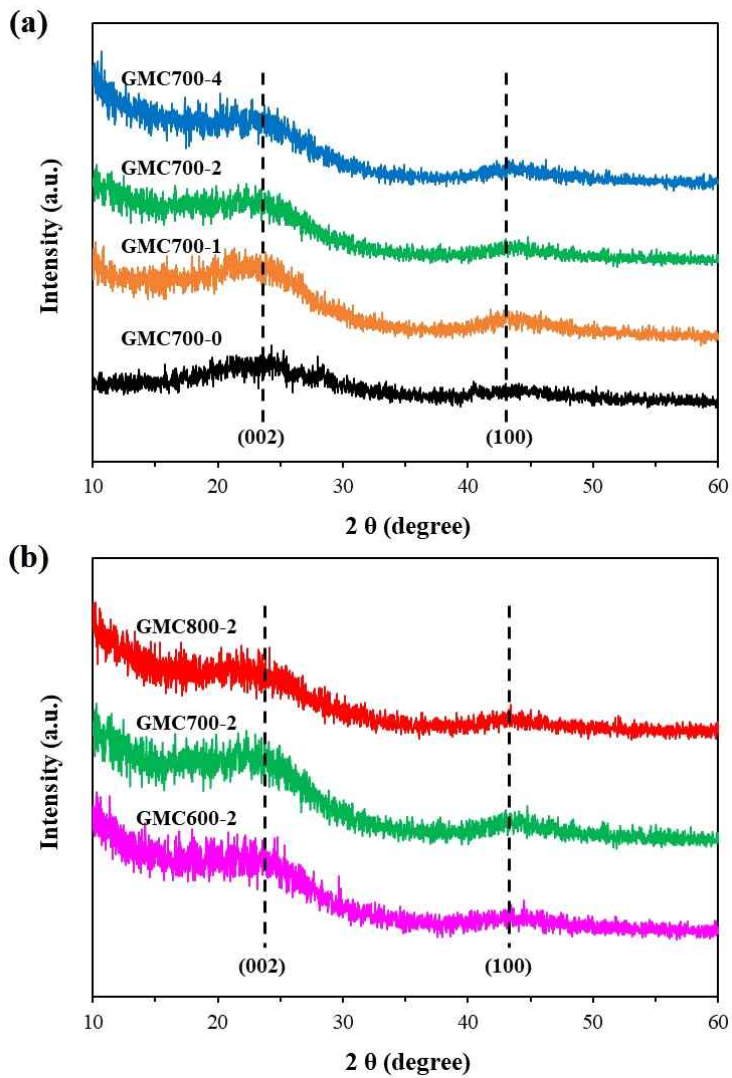
Figure 4.6. XRD spectra of GMCs depending on ZnCl$_2$ impregnation ratio (a) and activation temperatures (b).

4.1.5. Raman spectroscopy

To identity the structural changes of carbon samples, Raman spectra was obtained for GMCs depending on $ZnCl_2$ impregnation ratio and activation temperatures. The result showed a well-known D-band attributed to defects and disordered portions of the carbon materials at approximately 1350 cm^{-1} and G-band related to the presence of ordered graphitic crystallites of carbon at 1580 cm^{-1}. As shown in Figure 4.7(a), the ratio of the D peak to G peak intensity ($R_I = I_D/I_G$) increased from 0.941 to 1.010 as the $ZnCl_2$/GM ratio increased because of the development of porous structure. In addition, the R_I values also increased from 0.945 to 1.060 in proportion to activation temperature. It showed the similar result in previous studies for activated carbon. Liu et al. [74] and Quach et al. [75] reported that the ratio of I_D/I_G increased with increasing activation temperature, on the other hand, the ratio of I_D/I_G reduced slightly above 900 °C because of rearrangement of the carbon crystallite under severe activation conditions. This result indicates that the GMCs mostly consisted of nongraphitized carbon. To clearly reveal the $ZnCl_2$ activation effects, the in-plane size (L_a) indicating the graphitic crystallite size was determined by the following equation:

$$L_a = 2.4 \times 10^{-10} \lambda^4 R_I^{-1} \tag{Eq. 4-1}$$

, where λ means the laser wavelength (nm) [23]. The calculated L_a values are shown in Table 4.2. The GMCs showed smaller L_a when the $ZnCl_2$/GM ratio and activation temperature increased, respectively. It is indicates that more defects were formed with a $ZnCl_2$/GM ratio of 4, which is in accordance with the previous BET result.
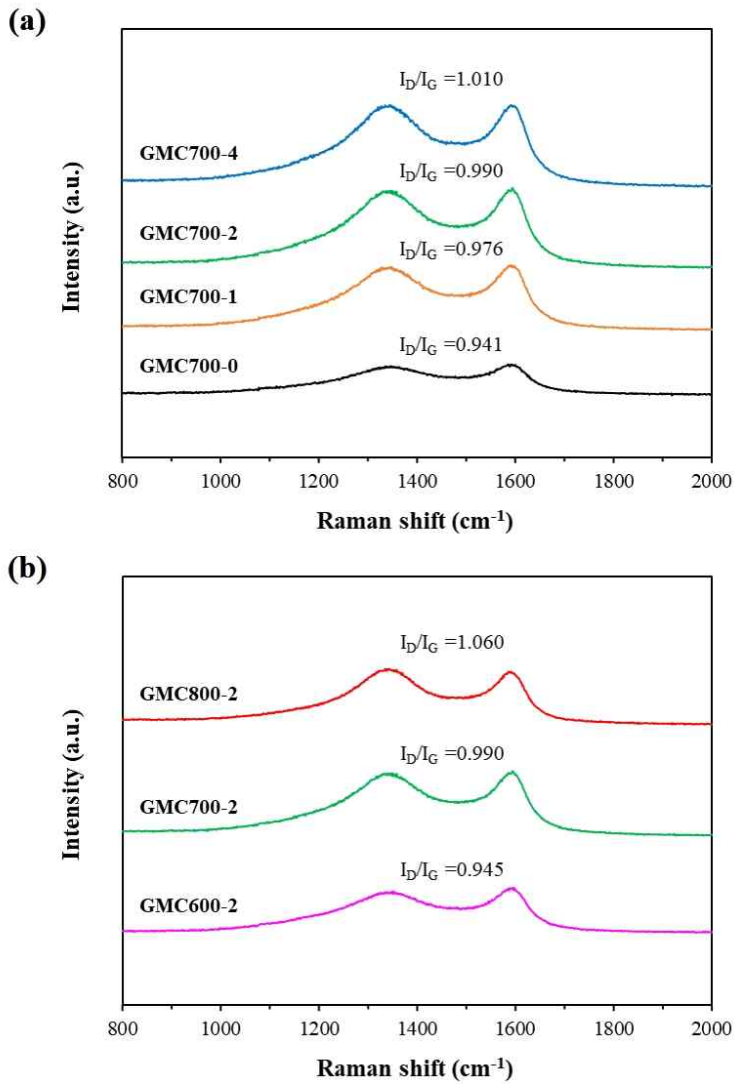
Figure 4.7. Raman spectra of GMCs depending on $ZnCl_2$ impregnation ratio (a) and activation temperatures (b).

Table 4.2. R_I and L_a values of GMCs.

Sample name	R_I	L_a (nm)
GMC700-0	0.941	20.4
GMC700-1	0.976	19.7
GMC700-2	0.990	19.4
GMC700-4	1.010	19.1
GMC600-2	0.945	20.4
GMC700-2	0.990	19.4
GMC800-2	1.060	18.2

4.1.6. Fourier transform infrared spectroscopy (FTIR)

FTIR was conducted to confirm the changes of the functional groups on GMC surface by $ZnCl_2$ activation. The FTIR spectra of GMC700-0, GMC700-1, GMC700-2 and GMC700-4 were shown in Figure 4.8. The band of O−H stretching vibration at 3420 cm^{-1} indicates the existence of surface hydroxyl groups or intrinsic moisture. The band located at 1600 cm^{-1} is attributed to the C−C stretching vibration in aromatic rings bands attributed to the decomposition of cellulose, hemicellulose and lignin in giant *Miscanthus* during activation. The band at 1100 cm^{-1} could be assigned to C−O vibration related to the ester, ethers, or phenol, alcohol group [42]. In addition, the Cl− containing functional group did not appear at the characteristic peak of 733 cm^{-1} [76], even though the giant *Miscanthus* was treated by $ZnCl_2$. In summary, generation of new peaks by $ZnCl_2$ activation was not found and the intensity of observed peaks was similar among GMCs. This result implies that $ZnCl_2$ activation do not give any effect on the changes of functional groups on GMC surfaces.
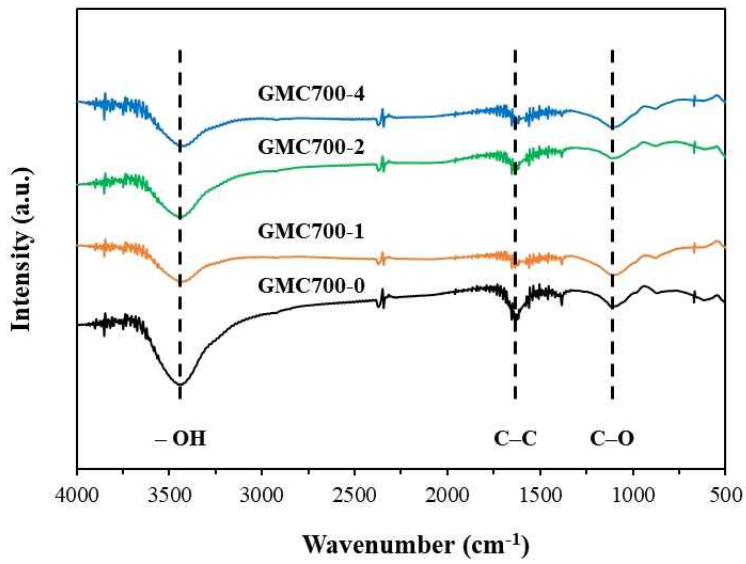
Figure 4.8. FTIR spectra of GMC700-0, GMC700-1, GMC700-2 and GMC700-4.

4.2. Electrochemical characteristics

4.2.1. Cyclic voltammetry (CV)

CV is an electrochemical technique to measure the current for the applied potential from an electrochemical cell. The direction of the potential is reversed at each end of applied potential range in CV curve. Current increases as the potential reached the reduction potential of the analyte. Likewise, current decreases as the analyte is depleted in the redox reaction.

To confirm the suitability as carbon electrodes, CV was conducted over the potential range of –0.5 to 0.5 V in a 1 M NaCl aqueous solution at different scan rates of 5, 10, 20, 50 and 100 mV s^{-1}. In addition, specific capacitance was calculated from the area of CV curves. As shown in Figure 4.9, CV curves of GMC electrodes showed a nearly rectangular shape at 5 mV s^{-1}, which followed typical EDLC behavior. As shown in Table 4.3, GMC700-2 possessed highest capacitance of 228 F g^{-1} at 5 mV s^{-1} among the GMC electrodes contrary to expectation that GMC700-4 will have more higher specific capacitance because of the largest BET surface. On the other hand, GMC700-1 and GMC600-2 had low specific capacitance, which is due to the limited ion-adsorption sites and poor ionic diffusion related to their nonporous structures. This result indicates that GMC700-2 is suitable for the EDLC electrode in a 1 M NaCl electrolyte.

The capacitance dependence on the scan rate was further examined for the GMC electrodes. Generally, capacitance decreased as the scan rate increased because the time ions diffuse into pores is enough at low scan rate as shown in Figure 4.10. Especially, GMC700-2 and GMC700-4 showed change of current as low as CEP21KS when the scan rate increased. This result explains that intrinsic properties of carbon materials remained regardless of the scan rate and there is a less influence by surface reaction.
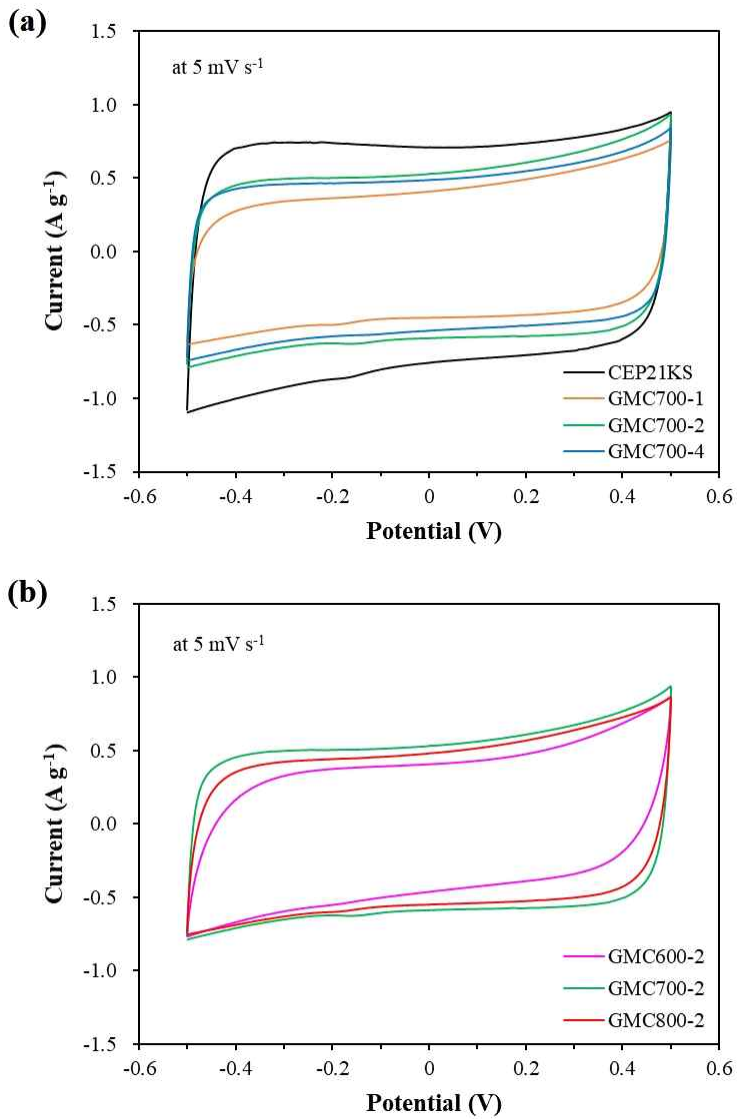
Figure 4.9. CV curves of carbon electrodes at a scan rate of 5 mV s^{-1} depending on ZnCl$_2$/GM ratio (a) and activation temperatures (b).
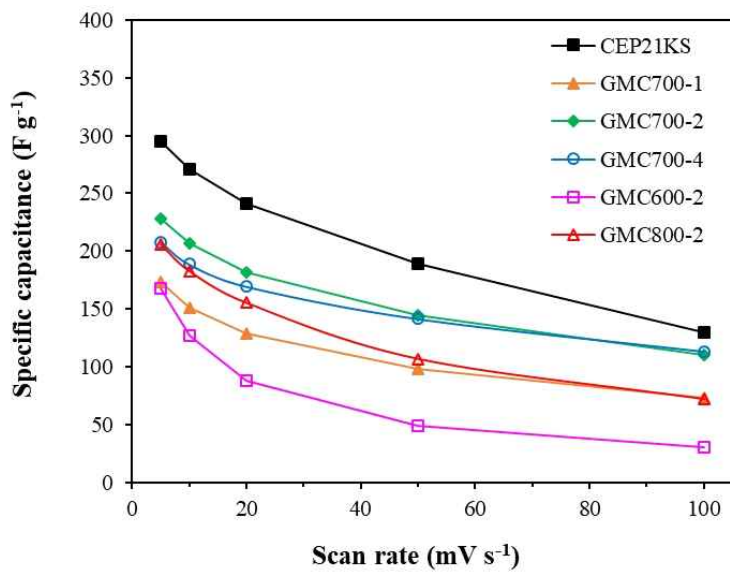
Figure 4.10. Specific capacitances of the carbon electrodes at different scan rates.

Table 4.3 Specific capacitances of the carbon electrodes at different scan rates.

C_{CV} (F g^{-1})	5 mV s^{-1}	10 mV s^{-1}	20 mV s^{-1}	50 mV s^{-1}	100 mV s^{-1}
CEP21KS	295	271	241	189	130
GMC700-1	173	151	129	98	73
GMC700-2	228	206	182	144	110
GMC700-4	208	189	170	142	113
GMC600-2	167	127	88	49	31
GMC800-2	206	183	155	107	72

4.2.2. Chronoamperometry (CA)

As mentioned in chapter 2, CA is an electrochemical technique to measure the current of the electrode as the potential step is applied. CA was performed applying potential step from 0 to 0.15 V for 3 min in 0.01 M NaCl electrolyte solution.

Figure 4.11 shows results of CA depending on $ZnCl_2$/GM ratio (a) and activation temperature (b). The GMC700-2 and GMC700-4 showed similar behavior to CEP21KS however GMC700-1 had lower current in charge/discharge. This result was similar to the specific capacitance by CV and the result depending on activation temperature showed similar tendency.

In addition, to estimate the diffusion coefficient of electrolyte ions on the electrode surface, the results of the CA were applied to the Cottrell equation:

$$i = \frac{nFAD^{1/2}C}{\sqrt{\pi t}}$$

(Eq. 4-2)

, where i is the current (A), n is the number of electrons involved in the reaction, F is the Faraday constant (C mol^{-1}), A is the area of the electrode (cm^2), D is the diffusion coefficient (cm^2 s^{-1}), C is the initial concentration of the analyte (mol cm^{-3}) and t is the time (s). The time range of 0.3 – 3 sec was adopted to calculate the diffusion coefficient and CA data were plotted for i vs $\pi t^{-1/2}$. The value of D can be calculated from the slope of Cottrell equation. As shown in Table 4.4, the diffusion coefficients determined from Cottrell equation were in the range of 7.6×10^{-12} – 1.9×10^{-11} m^2 s^{-1}. The D value of GMCs were higher than CEP21KS, which indicates that efficient mass transfer of electrolyte ions occurs on the electrode surface.
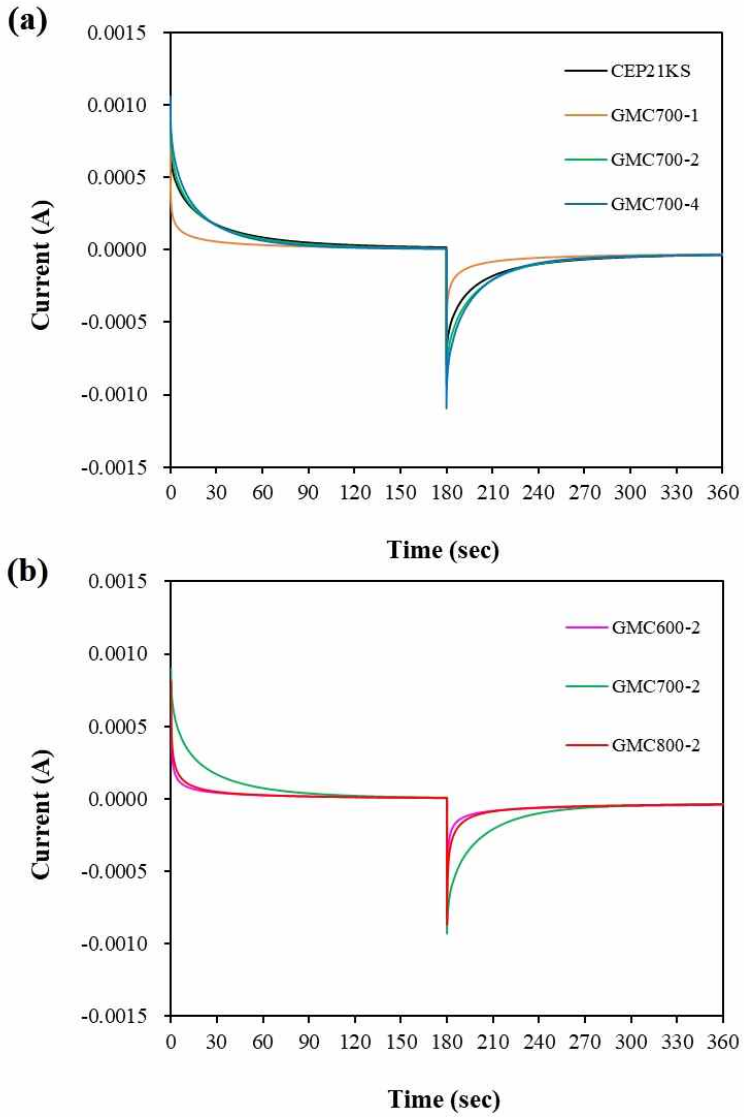
Figure 4.11. Chronoamperogram of carbon electrodes depending on ZnCl$_2$/GM ratio (a) and activation temperatures (b).

Table 4.4. Diffusion coefficients (D) determined from Cottrell equation.

Samples	D (m^2 s^{-1})	r^2
CEP21KS	7.62×10^{-12}	0.950
GMC700-1	8.30×10^{-12}	0.988
GMC700-2	1.30×10^{-11}	0.952
GMC700-4	1.62×10^{-11}	0.944
GMC600-2	1.57×10^{-11}	0.995
GMC800-2	1.93×10^{-11}	0.987

4.2.3. Electrochemical impedance spectroscopy (EIS)

EIS has been employed to evaluate several electrochemical properties of the electrodes and provides information about the electrochemical reactions that occur on the electrodes. To estimate the impedance in a electrochemical cell, EIS measurement was conducted. As shown in Figure 4.12, the Nyquist plots display semicircle at high frequency and a straight line at low frequency. The intercept at high-frequency on the real axis indicates the sum of the resistances. They are the intrinsic resistance of the electrolyte, resistance of the electrode material, and the contact resistance between the electrode material and the current collector [77].

Figure 4.13 shows the Nyquist plots of the GMC electrodes in the 1 M NaCl electrolyte and an AC circuit model. As shown in Table 4.5, the intrinsic resistance of GMCs was less than 3 Ω, which is comparable to carbon materials derived from biomass [46,49]. The semicircle behavior is related to the porous structure of the working electrodes. R1 implies the resistance between the electrolyte solution and the electrode material. R1 of the biocarbon electrodes were in the range of 3.36×10^{4} – 4.59×10^{4} Ω. The higher values of R1 indicate that there was high resistance between the electrolyte solution and the electrode material because of binder. Further systematic studies are required for higher mass transport of ions on thin carbon electrodes.
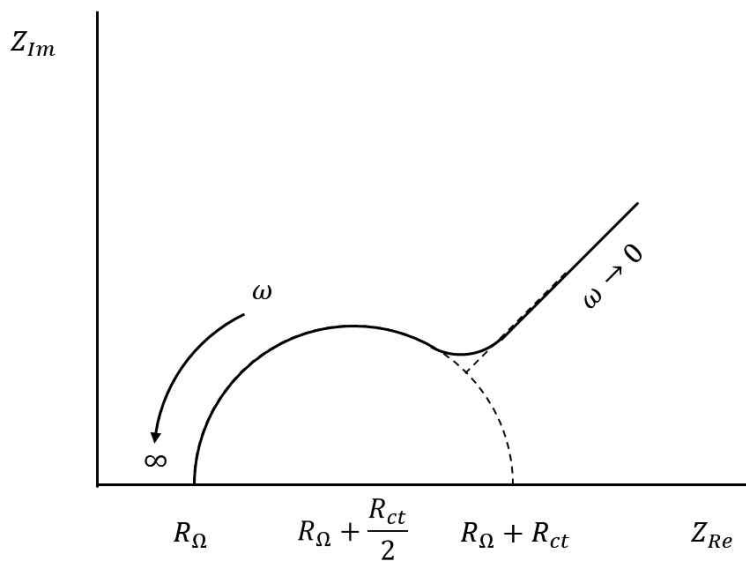
Figure 4.12. Nyquist plot of the electrochemical cell.

(a)

(b)

(c)
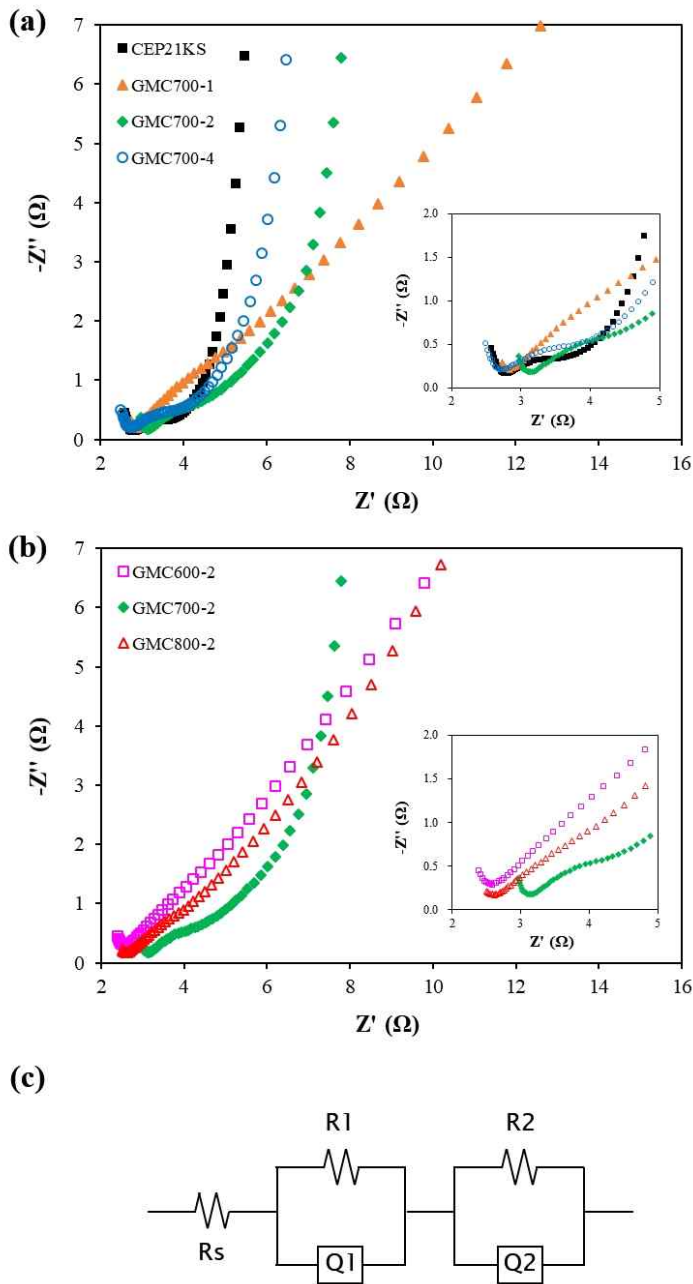
Figure 4.13. Nyquist plots of the carbon electrodes depending on $ZnCl_2$ impregnation ratio (a) and (b) activation temperatures (b), and the AC circuit model (c).

Table 4.5. AC impedance parameters of carbon electrodes.

Parameters	CEP21KS	GMC700-1	GMC700-2	GMC700-4	GMC600-2	GMC800-2
Rs (Ω)	1.60	2.49	2.59	1.72	1.68	2.28
R1 (Ω)	3.36×10^4	4.59×10^4	3.75×10^4	4.12×10^4	3.46×10^4	3.60×10^4
Q1	0.28	0.14	0.16	0.21	0.17	0.08
R2 (Ω)	7.08×10^4	957	319	6.5×10^5	6.75×10^4	528
Q2	0.27	0.04	0.18	0.15	0.02	0.08

4.3. Performance of CDI

CDI experiments depending on different flow rate were carried out at 100 mg L^{-1} of NaCl and 1.2 V using the CEP21KS electrode. Figure 4.14(a) describes adsorption results for NaCl at the different flow rate (15 – 30 mL min^{-1}). When the flow rate decreased, reaching to equilibrium became long, on the other hand concentration of NaCl was more reduced. This result indicates that a time ions can be adsorbed is not sufficient as the flow rate increase, and a time electrolyte solution to connect with electrode surface enough is required. Based on this result, subsequent experiments were conducted at 15 mL min^{-1} of flow rate. Figure 4.14(b) shows CDI results of the different carbon electrodes during three adsorption/desorption cycles and all carbon electrodes showed excellent reproducibility. Figure 4.15(a) and (c) describe adsorption/desorption behavior of GMC700-4 at different applied potentials and different concentrations of NaCl, respectively. As shown in Figure 4.15(b), difference of equilibrium time by applied potential was insignificant. On the other hand, equilibrium time became short as the concentration of NaCl increased. This result indicates that adsorption kinetics is more affected by concentration of feed water than applied potential.
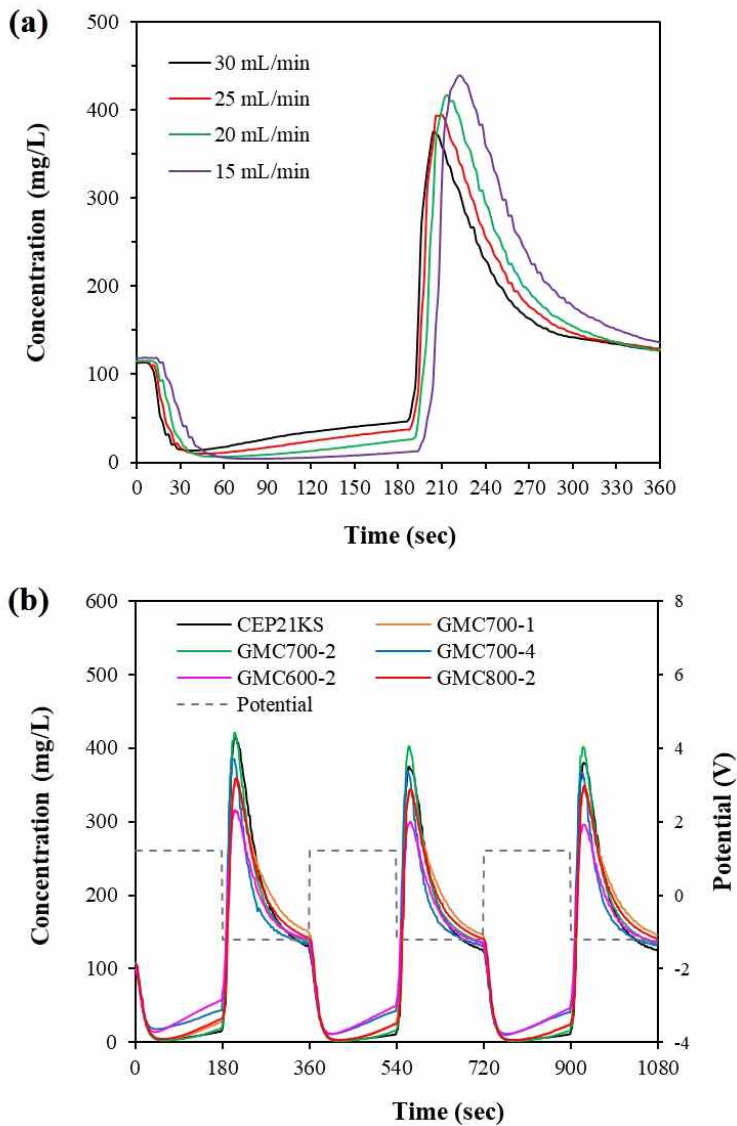
Figure 4.14. Concentration responses at different flow rates using CEP21KS (a) and CDI performances of the carbon electrodes (b) at 100 mg L^{-1} of NaCl and 1.2 V.
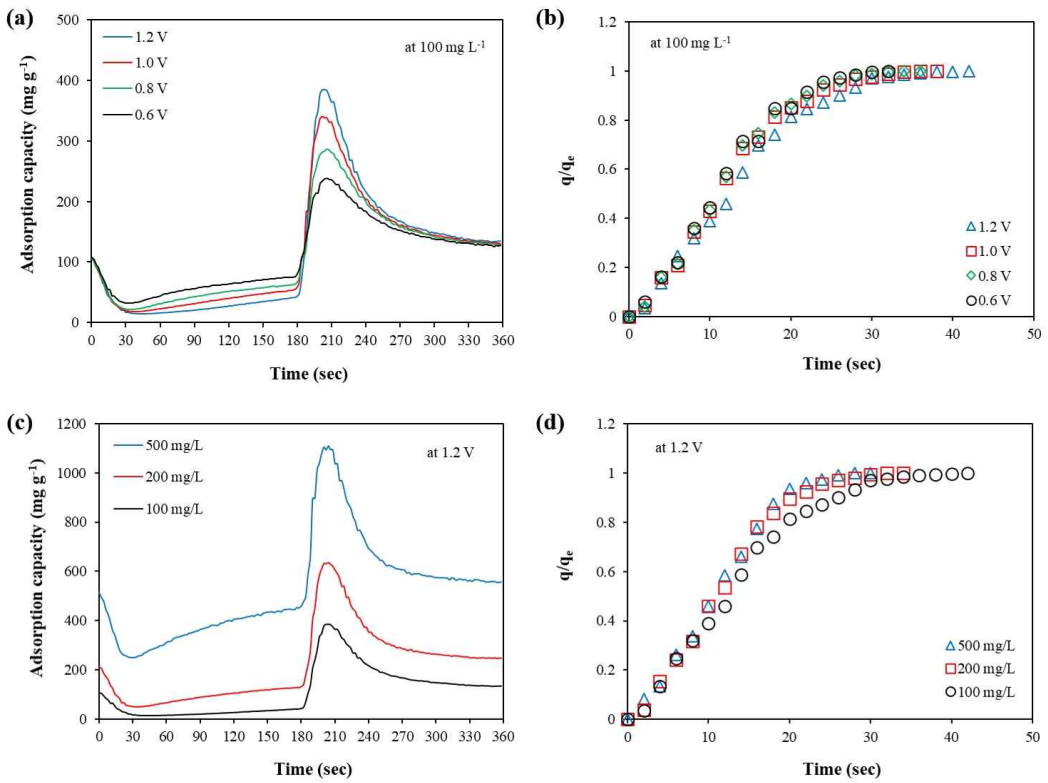
Figure 4.15. Adsorption/desorption curves of GMC700-4: effects of the applied potential (a, b) and NaCl concentration (c, d).

4.3.1. Electrosorption kinetics

Kinetic modeling is useful for investigate the characteristics of adsorption process. Identification of equilibrium time and the mechanism of adsorption were conducted. The experimental data for NaCl were applied to the various kinetic models such as pseudo-first-order, pseudo-second-order, Weber-Morris, Urano-Tachikawa and S-shape models. Kinetic model parameters were calculated using MATLAB 2021a with nonlinear regression method. The kinetic models of CEP21KS and GMC700-4 for 100 mg L^{-1} of NaCl at 1.2 V are shown in Figure 4.16 and the values of kinetic parameters are described in Table 4.6. The kinetic data are well agreed with the S-shape model, which was confirmed by higher r^2 value calculated by following equation:

$$r^2 = 1 - \frac{\sum_{i=1}^{N}(q_{exp,i} - q_{cal,i})}{\sum_{i=1}^{N}(q_{exp,i} - \bar{q}_{exp,i})} \qquad \text{(Eq. 4-3)}$$

Contrary to expectation, other kinetic models except for S-shape equation were not successfully applied to simulate the kinetic data as shown in Figure 4.16.
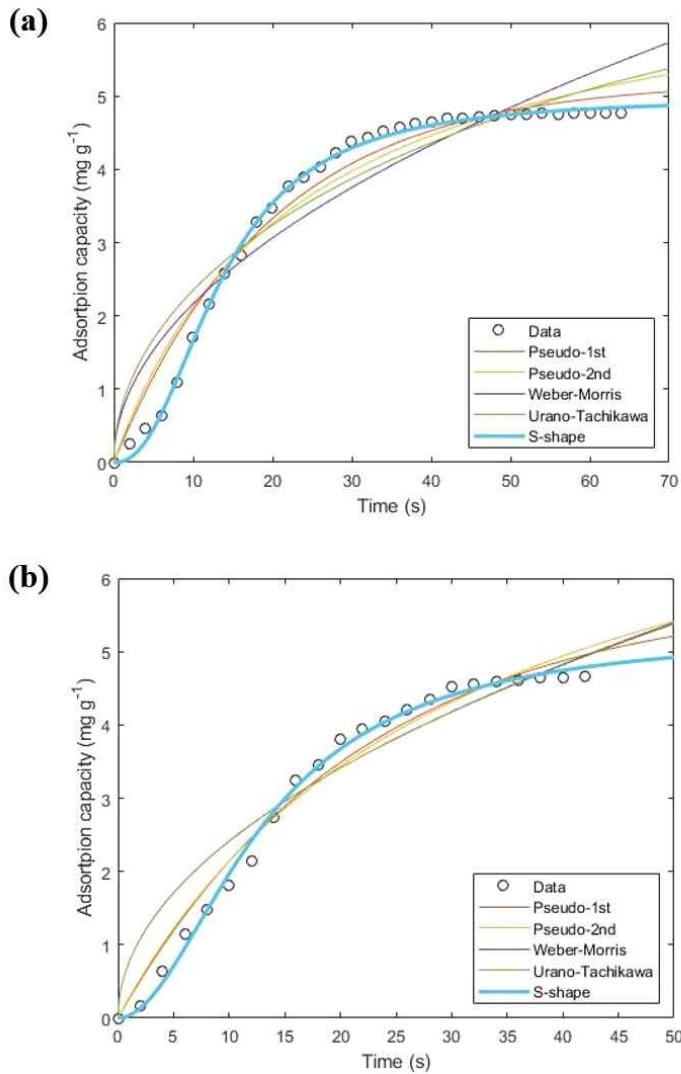
Figure 4.16. Kinetic models of CEP21KS (a) and GMC700-4
(b) at 100 mg L^{-1} of NaCl and 1.2 V.

Table 4.6. Kinetic parameters of CEP21KS and GMC700-4.

Model	Parameter	CEP21KS	GMC700-4
Pseudo-first-order	q_e (mg g^{-1})	5.21	5.79
	k_1 (s^{-1})	5.10×10^{-2}	4.61×10^{-2}
	r^2	0.971	0.979
Pseudo-second-order	q_e (mg g^{-1})	7.05	8.77
	k_2 (g mg^{-1} s^{-1})	6.10×10^{-3}	3.70×10^{-3}
	r^2	0.955	0.973
Weber-Morris	K_i (mg g^{-1} s$^{-0.5}$)	0.6849	0.7631
	r^2	0.895	0.922
Urano-Tachikawa	q_e (mg g^{-1})	7.47	2356
	D_i (m^2 s^{-1})	2.37×10^{-13}	2.39×10^{-18}
	r^2	0.906	0.922
S-shape	q_e (mg g^{-1})	4.98	5.29
	n	0.4351	0.5151
	b (s^{-1})	2.50×10^{-3}	6.80×10^{-3}
	r^2	0.998	0.995

4.3.2. Electrosorption isotherms

As mentioned in chapter 2, adsorption isotherm modeling is useful to understand the mechanism of the adsorption process. The adsorption equilibrium experiment was carried out in the NaCl concentration range of 100 to 2000 mg L^{-1} at 1.2V. The maximum salt adsorption capacity was 21.9 mg g^{-1} for GMC700-4, which was similar result for CEP21KS (24.5 mg g^{-1}). It is clear that the biomass carbon electrode showed excellent performance as much as the commercial carbon material.

In addition, to evaluate parameters of each adsorption isotherm model and to confirm the best fit model for understanding adsorption mechanism, MATLAB 2021a was employed with nonlinear regression method. Figure 4.17 shows various isotherm models for CEP21KS and GMC700-4 at 1.2 V. The determined parameters of each adsorption isotherm model are summarized in Table 4.7. The adsorption equilibrium data were fitted well to the Sips isotherm model, which was confirmed by high r^2 value. Figure 4.18 illustrates the isotherms of GMCs depending on the $ZnCl_2$/GM ratio and activation temperatures. Here, the solid lines are the results of the simulated with Sips isotherm. The estimated isotherm parameters of the Sips equation are summarized in Table 4.8. The Sips isotherm parameters of q_{m_S}, n_S, K_S were in the range of 13.4 – 30.8 mg g^{-1}, 1.2367 – 2.0601, 0.0175 – 0.0853 L mg^{-1}, respectively.
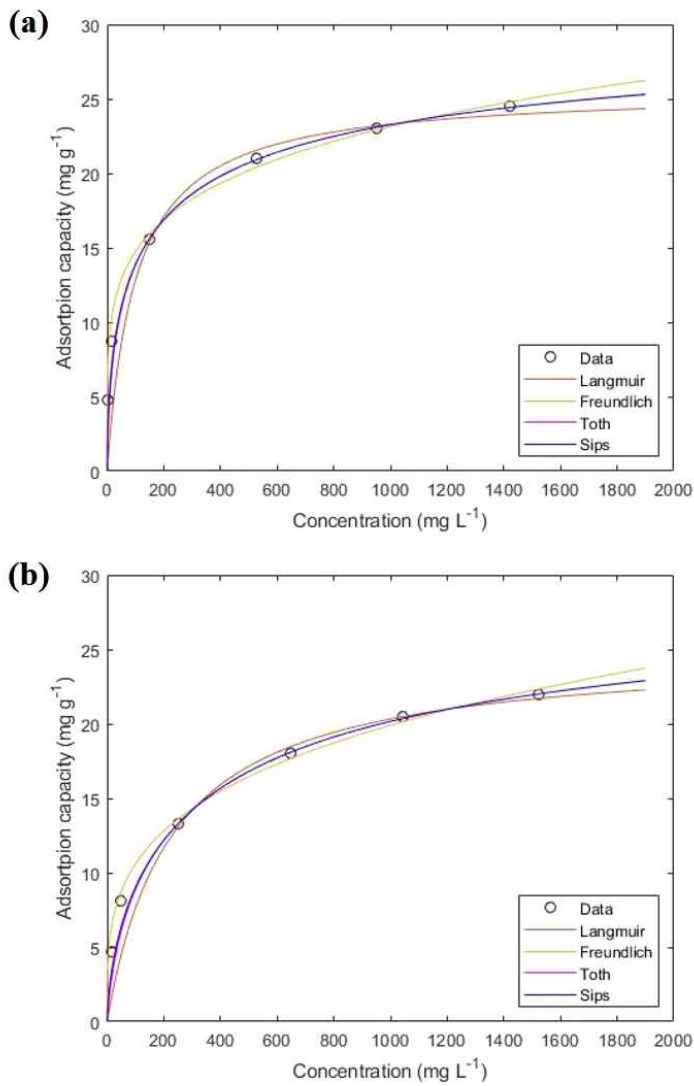
Figure 4.17. Isotherms of CEP21KS (a) and GMC700-4 (b) at 1.2 V.

Table 4.7. Isotherm parameters of CEP21KS and GMC700-4.

Model	Parameter	CEP21KS	GMC700-4
Langmuir	q_{m_L} (mg g^{-1})	25.6	25.0
	K_L (L mg^{-1})	1.00×10^{-2}	4.40×10^{-2}
	r^2	0.984	0.992
Freundlich	n_F	5.0968	3.6457
	K_F (L mg^{-1})	5.9679	2.9931
	r^2	0.988	0.989
Toth	q_{m_T} (mg g^{-1})	33.7	32.8
	n_T	0.4325	0.5315
	K_T (L mg^{-1})	5.76×10^{-2}	9.90×10^{-2}
	r^2	1.000	0.999
Sips	q_{m_S} (mg g^{-1})	31.9	30.8
	n_S	1.8392	1.5130
	K_S (L mg^{-1})	6.29×10^{-2}	1.97×10^{-2}
	r^2	1.000	0.999
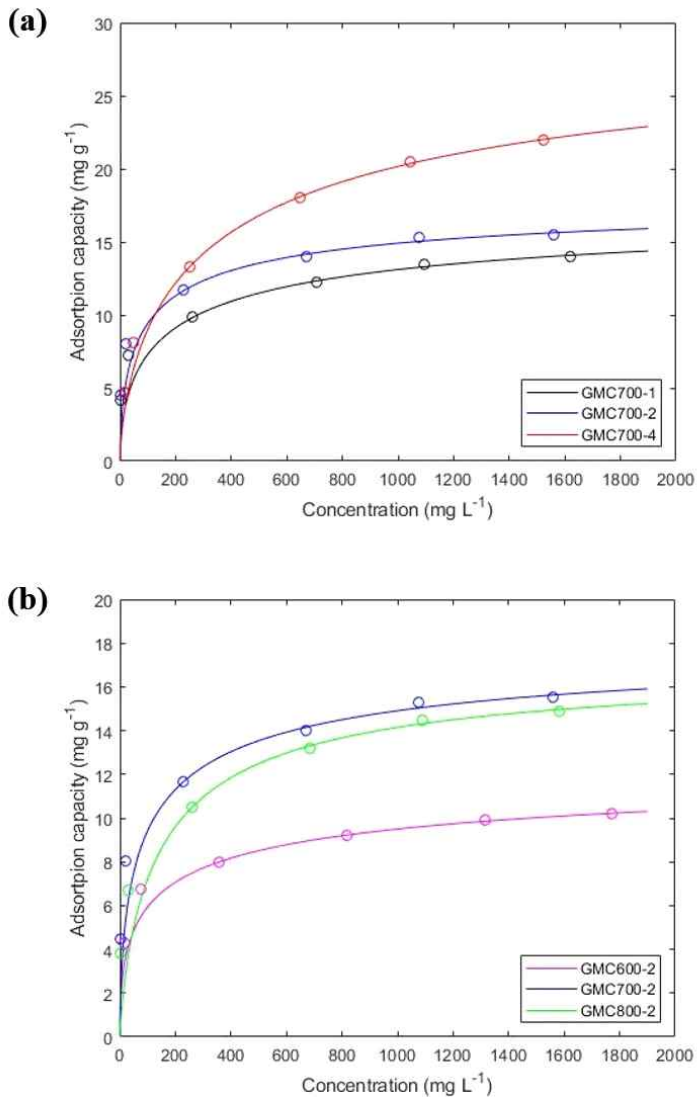
Figure 4.18. Sips isotherms of GMC electrodes: effects of ZnCl$_2$/GM ratio (a) and activation temperatures (b) at 1.2 V.

Table 4.8. Sips isotherm parameters of GMC electrodes.

	GMC700-1	GMC700-2	GMC700-4
q_{m_S} (mg g^{-1})	18.3	18.6	30.8
n_S	1.7286	1.6770	1.5130
K_S (L mg^{-1})	4.62×10^{-2}	6.60×10^{-2}	1.97×10^{-2}
r^2	0.994	0.988	0.999
	GMC600-2	GMC700-2	GMC800-2
q_{m_S} (mg g^{-1})	13.4	18.6	17.2
n_S	2.0601	1.6770	1.2367
K_S (L mg^{-1})	8.53×10^{-2}	6.60×10^{-2}	1.75×10^{-2}
r^2	0.999	0.988	0.996

Chapter 5. Conclusions

The design, preparation, characterization and application of the porous biocarbons are the goal of this work. Porous biocarbons were prepared from giant *Miscanthus* (GM) through carbonization and activation processes using zinc chloride. Porous biocarbons showed excellent electrochemical property and higher salt adsorption capacity. The adsorption kinetic data were analyzed with various models including pseudo-first-order, pseudo-second-order, Weber-Morris, Urano-Tachikawa and S-shape equations. In addition, the adsorption equilibrium data were fitted with many adsorption isotherms such as Langmuir, Freundlich, Toth and Sips equations.

Based on the experimental data and theoretical approach, the results can be summarized as follows:

(1) Porous biocarbons from giant *Miscanthus* were successfully prepared by carbonization and activation with zinc chloride under the different conditions of $ZnCl_2$/GM ratio (1, 2, 4) and activation temperatures (600, 700, 800 °C).

(2) The specific surface area and average pore size of the porous biocarbons were in the range of 994 – 1661 m^2 g^{-1} and around 2 nm under different activation conditions, respectively. Nitrogen adsorption and desorption isotherms were type I according to IUPAC classification. In addition, Raman spectra showed the increase of R_I values with $ZnCl_2$/GM and activation temperatures. This result implies the well-developed surface roughness and pore structures.

(3) The electrochemical properties of carbon electrodes were characterized by cyclic voltammetry, chronoamperometry and electrochemical impedance spectroscopy. The specific capacitances from cyclic voltammograms were in the range of 167 – 228 F g^{-1} at 5 mV s^{-1} of scan rate. The analytical solution (i.e., Cottrell equation) of the parabolic partial differential equations for the ion transport on carbon electrodes was obtained by Laplace transformation. The diffusion coefficients determined from Cottrell equation were in the range of 8.30 × 10^{-12} – 1.93 × 10^{-11} m^2 s^{-1}.

(4) The adsorption and desorption curves under key operating conditions showed excellent reproducibility. The maximum salt adsorption capacity was 21.9 mg g^{-1} under the conditions of NaCl concentration of 2000 mg L^{-1} and applied potential of 1.2 V. In addition, S-shape kinetic model and Sips isotherm were well fitted the experimental data under the different conditions of applied potentials and concentrations.

In summary, the present study may conclude that the porous biocarbon electrodes prepared from giant *Miscanthus* are adequate for capacitive deionization to remove dissolved ions from water and wastewater. The advanced capacitive deionization processes combined with solar energy, reverse osmosis membrane, microfiltration, microbial fuel cell and photocatalyst will be continued.

Reference

1. Luciano, M. A.; Ribeiro, H.; Bruch, G. E.; Silva, G. G., Efficiency of capacitive deionization using carbon materials based electrodes for water desalination. *Journal of Electroanalytical Chemistry* **2020,** *859*.

2. Xing, W.; Liang, J.; Tang, W.; He, D.; Yan, M.; Wang, X.; Luo, Y.; Tang, N.; Huang, M., Versatile applications of capacitive deionization (CDI)-based technologies. *Desalination* **2020,** *482*.

3. Lu, T.; Liu, Y.; Xu, X.; Pan, L.; Alothman, A. A.; Shapter, J.; Wang, Y.; Yamauchi, Y., Highly efficient water desalination by capacitive deionization on biomass-derived porous carbon nanoflakes. *Separation and Purification Technology* **2021,** *256*.

4. Tang, W.; Liang, J.; He, D.; Gong, J.; Tang, L.; Liu, Z.; Wang, D.; Zeng, G., Various cell architectures of capacitive deionization: Recent advances and future trends. *Water Res* **2019,** *150*, 225-251.

5. Landon, J.; Gao, X.; Omosebi, A.; Liu, K., Progress and outlook for capacitive deionization technology. *Current Opinion in Chemical Engineering* **2019,** *25*, 1-8.

6. Porada, S.; Zhao, R.; van der Wal, A.; Presser, V.; Biesheuvel, P. M., Review on the science and technology of water desalination by capacitive deionization. *Progress in Materials Science* **2013,** *58* (8), 1388-1442.

7. Bales, C.; Kovalsky, P.; Fletcher, J.; Waite, T. D., Low cost desalination of brackish groundwaters by Capacitive Deionization (CDI) – Implications for irrigated agriculture. *Desalination* **2019,** *453*, 37-53.

8. Lee, J.-H.; Choi, J.-H., The production of ultrapure water by membrane capacitive deionization (MCDI) technology. *Journal of Membrane Science* **2012,** *409-410*, 251-256.

9. Bao, S.; Duan, J.; Zhang, Y., Recovery of V(V) from complex vanadium solution using capacitive deionization (CDI) with resin/carbon composite electrode. *Chemosphere* **2018,** *208*, 14-20.

10. Laxman, K.; Sathe, P.; Al Abri, M.; Dobretsov, S.; Dutta, J., Disinfection of Bacteria in Water by Capacitive Deionization. *Front Chem* **2020,** *8*, 774.

11. Hou, S.; Xu, X.; Wang, M.; Lu, T.; Sun, C. Q.; Pan, L., Synergistic conversion and removal of total Cr from aqueous solution by photocatalysis and capacitive deionization. *Chemical Engineering Journal* **2018,** *337*, 398-404.

12. Liang, P.; Yuan, L.; Yang, X.; Huang, X., Influence of circuit arrangement on the performance of a microbial fuel cell driven capacitive deionization (MFC-CDI) system. *Desalination* **2015,** *369*, 68-74.

13. Legrand, L.; Schaetzle, O.; de Kler, R. C. F.; Hamelers, H. V. M., Solvent-Free CO_2 Capture Using Membrane Capacitive Deionization. *Environ Sci Technol* **2018,** *52* (16), 9478-9485.

14. Suss, M. E.; Porada, S.; Sun, X.; Biesheuvel, P. M.; Yoon, J.; Presser, V., Water desalination via capacitive deionization: what is it and what can we expect from it? *Energy & Environmental Science* **2015,** *8* (8), 2296-2319.

15. Hu, C.; Liu, F.; Lan, H.; Liu, H.; Qu, J., Preparation of a manganese dioxide/carbon fiber electrode for electrosorptive removal of copper ions from water. *J Colloid Interface Sci* **2015,** *446*, 359-65.

16. Zornitta, R. L.; Srimuk, P.; Lee, J.; Krüner, B.; Aslan, M.; Ruotolo, L. A. M.; Presser, V., Charge and Potential Balancing for Optimized Capacitive Deionization Using Lignin-Derived, Low-Cost Activated Carbon Electrodes. *ChemSusChem* **2018,** *11* (13), 2101-2113.

17. Oren, Y., Capacitive deionization (CDI) for desalination and water treatment — past, present and future (a review). *Desalination* **2008,** *228* (1-3), 10-29.

18. Choi, J.-H., Fabrication of a carbon electrode using activated carbon powder and application to the capacitive deionization process. *Separation and Purification Technology* **2010,** *70* (3), 362-366.

19. Xie, Z.; Cheng, J.; Yan, J.; Cai, W.; Nie, P.; Chan, H. T. H.; Liu, J., Polydopamine Modified Activated Carbon for Capacitive Desalination. *Journal of The Electrochemical Society* **2017,** *164* (12), A2636-A2643.

20. Zhang, D.; Shi, L.; Fang, J.; Dai, K., Influence of diameter of carbon nanotubes mounted in flow-through capacitors on removal of NaCl from salt water. *Journal of Materials Science* **2007,** *42* (7), 2471-2475.

21. El-Deen, A. G.; Barakat, N. A. M.; Khalil, K. A.; Kim, H. Y., Hollow carbon nanofibers as an effective electrode for brackish water desalination using the capacitive deionization process. *New J. Chem.* **2014,** *38* (1), 198-205.

22. Dong, Q.; Wang, G.; Qian, B.; Hu, C.; Wang, Y.; Qiu, J., Electrospun Composites Made of Reduced Graphene Oxide and Activated Carbon Nanofibers for Capacitive Deionization. *Electrochimica Acta* **2014,** *137*, 388-394.

23. Xu, P.; Drewes, J. E.; Heil, D.; Wang, G., Treatment of brackish produced water using carbon aerogel-based capacitive deionization technology. *Water Res* **2008,** *42* (10-11), 2605-17.

24. Gabelich, C. J.; Tran, T. D.; Suffet, I. H. M., Electrosorption of Inorganic Salts from Aqueous Solution Using Carbon Aerogels. *Environmental Science & Technology* **2002,** *36* (13), 3010-3019.

25. Zhao, C.; Liu, G.; Sun, N.; Zhang, X.; Wang, G.; Zhang, Y.; Zhang, H.; Zhao, H., Biomass-derived N-doped porous carbon as electrode materials for Zn-air battery powered capacitive deionization. *Chemical Engineering Journal* **2018,** *334*, 1270-1280.

26. Xu, D.; Tong, Y.; Yan, T.; Shi, L.; Zhang, D., N,P-Codoped Meso-/Microporous Carbon Derived from Biomass Materials via a Dual-Activation Strategy as High-Performance Electrodes for Deionization Capacitors. *ACS Sustainable Chemistry & Engineering* **2017,** *5* (7), 5810-5819.

27. Zhang, J.; Fang, J.; Han, J.; Yan, T.; Shi, L.; Zhang, D., N, P, S co-doped hollow carbon polyhedra derived from MOF-based core–shell nanocomposites for capacitive deionization. *Journal of Materials Chemistry A* **2018,** *6* (31), 15245-15252.

28. Wang, H.; Yan, T.; Shi, L.; Chen, G.; Zhang, J.; Zhang, D., Creating Nitrogen-Doped Hollow Multiyolk@Shell Carbon as High Performance Electrodes for Flow-Through Deionization Capacitors. *ACS Sustainable Chemistry & Engineering* **2017,** *5* (4), 3329-3338.

29. Wang, H.; Shi, L.; Yan, T.; Zhang, J.; Zhong, Q.; Zhang, D., Design of graphene-coated hollow mesoporous carbon spheres as high performance electrodes for capacitive deionization. *Journal of Materials Chemistry A* **2014,** *2* (13), 4739-4750.

30. Liu, P.; Yan, T.; Shi, L.; Park, H. S.; Chen, X.; Zhao, Z.; Zhang, D., Graphene-based materials for capacitive deionization. *Journal of Materials Chemistry A* **2017,** *5* (27), 13907-13943.

31. Li, H.; Pan, L.; Nie, C.; Liu, Y.; Sun, Z., Reduced graphene oxide and activated carbon composites for capacitive deionization. *Journal of Materials Chemistry* **2012,** *22* (31), 15556-15561.

32. Khan, Z. U.; Yan, T.; Shi, L.; Zhang, D., Improved capacitive deionization by using 3D intercalated graphene sheet–sphere nanocomposite architectures. *Environmental Science: Nano* **2018,** *5* (4), 980-991.

33. Duan, H.; Yan, T.; Chen, G.; Zhang, J.; Shi, L.; Zhang, D., A facile strategy for the fast construction of porous graphene frameworks and their enhanced electrosorption performance. *Chemical Communications* **2017,** *53* (54), 7465-7468.

34. Mo, R.-J.; Zhao, Y.; Wu, M.; Xiao, H.-M.; Kuga, S.; Huang, Y.; Li, J.-P.; Fu, S.-Y., Activated carbon from nitrogen rich watermelon rind for high-performance supercapacitors. *RSC Advances* **2016,** *6* (64), 59333-59342.

35. Ren, Y.; Zhang, J.; Xu, Q.; Chen, Z.; Yang, D.; Wang, B.; Jiang, Z., Biomass-derived three-dimensional porous N-doped carbonaceous aerogel for efficient supercapacitor electrodes. *RSC Advances* **2014,** *4* (45).

36. Hameed, B. H.; Rahman, A. A., Removal of phenol from aqueous solutions by adsorption onto activated carbon prepared from biomass material. *J Hazard Mater* **2008,** *160* (2-3), 576-81.

37. Hulicova-Jurcakova, D.; Seredych, M.; Lu, G. Q.; Bandosz, T. J., Combined Effect of Nitrogen- and Oxygen-Containing Functional Groups of Microporous Activated Carbon on its Electrochemical Performance in Supercapacitors. *Advanced Functional Materials* **2009,** *19* (3), 438-447.

38. Chen, J.; Zhou, X.; Mei, C.; Xu, J.; Zhou, S.; Wong, C.-P., Evaluating biomass-derived hierarchically porous carbon as the positive electrode material for hybrid Na-ion capacitors. *Journal of Power Sources* **2017,** *342*, 48-55.

39. Titirici, M.-M.; White, R. J.; Falco, C.; Sevilla, M., Black perspectives for a green future: hydrothermal carbons for environment protection and energy storage. *Energy & Environmental Science* **2012,** *5* (5), 6796-6822.

40. Dutta, S.; Bhaumik, A.; Wu, K. C. W., Hierarchically porous carbon derived from polymers and biomass: effect of interconnected pores on energy applications. *Energy & Environmental Science* **2014,** *7* (11), 3574-3592.

41. Mohammadinejad, R.; Karimi, S.; Iravani, S.; Varma, R. S., Plant-derived nanostructures: types and applications. *Green Chemistry* **2016,** *18* (1), 20-52.

42. Liu, J.; Wang, S.; Yang, J.; Liao, J.; Lu, M.; Pan, H.; An, L., $ZnCl_2$ activated electrospun carbon nanofiber for capacitive desalination. *Desalination* **2014,** *344*, 446-453.

43. Cen, B.; Yang, R.; Li, K.; Lv, C.; Liang, B., Large capacity and rapid rate of ion removal from synthetic municipal wastewater via CDI using chitosan-based nitrogen-doped porous carbon electrode. *Process Safety and Environmental Protection* **2021,** *147*, 857-865.

44. Muthukumaraswamy Rangaraj, V.; Achazhiyath Edathil, A.; Y. Kannangara, Y.; Song, J.-K.; Abu Haija, M.; Banat, F., Tamarind shell derived N-doped carbon for capacitive deionization (CDI) studies. *Journal of Electroanalytical Chemistry* **2019,** *848*.

45. Hai, A.; Bharath, G.; Babu, K. R.; Taher, H.; Naushad, M.; Banat, F., Date seeds biomass-derived activated carbon for efficient removal of NaCl from saline solution. *Process Safety and Environmental Protection* **2019,** *129*, 103-111.

46. Xing, W.; Zhang, M.; Liang, J.; Tang, W.; Li, P.; Luo, Y.; Tang, N.; Guo, J., Facile synthesis of pinecone biomass-derived phosphorus-doping porous carbon electrodes for efficient electrochemical salt removal. *Separation and Purification Technology* **2020,** *251*.

47. Xie, Z.; Shang, X.; Yan, J.; Hussain, T.; Nie, P.; Liu, J., Biomass-derived porous carbon anode for high-performance capacitive deionization. *Electrochimica Acta* **2018,** *290*, 666-675.

48. Maniscalco, M. P.; Corrado, C.; Volpe, R.; Messineo, A., Evaluation of the optimal activation parameters for almond shell bio-char production for capacitive deionization. *Bioresource Technology Reports* **2020,** *11*.

49. Kyaw, H. H.; Al-Mashaikhi, S. M.; Myint, M. T. Z.; Al-Harthi, S.; El-Shafey, E.-S. I.; Al-Abri, M., Activated carbon derived from the date palm leaflets as multifunctional electrodes in capacitive deionization system. *Chemical Engineering and Processing - Process Intensification* **2021,** *161*.

50. Liu, S.-H.; Tang, Y.-H., Hierarchically porous biocarbons prepared by microwave-aided carbonization and activation for capacitive deionization. *Journal of Electroanalytical Chemistry* **2020,** *878*.

51. Liu, Q.; Li, X.; Wu, Y.; Qing, M.; Tan, G.; Xiao, D., Pine pollen derived porous carbon with efficient capacitive deionization performance. *Electrochimica Acta* **2019,** *298*, 360-371.

52. Bedia, J.; Peñas-Garzón, M.; Gómez-Avilés, A.; Rodriguez, J. J.; Belver, C., Review on Activated Carbons by Chemical Activation with $FeCl_3$. *C — Journal of Carbon Research* **2020,** *6* (2).

53. Cruz-Olivares, J.; Pérez-Alonso, C.; Barrera-Díaz, C.; Natividad, R.; Chaparro-Mercado, M. C., Thermodynamical and analytical evidence of lead ions chemisorption onto Pimenta dioica. *Chemical Engineering Journal* **2011,** *166* (3), 814-821.

54. Özacar, M.; Şengil, İ. A., A kinetic study of metal complex dye sorption onto pine sawdust. *Process Biochemistry* **2005,** *40* (2), 565-572.

55. Loukidou, M. X.; Zouboulis, A. I.; Karapantsios, T. D.; Matis, K. A., Equilibrium and kinetic modeling of chromium(VI) biosorption by Aeromonas caviae. *Colloids and Surfaces A: Physicochemical and Engineering Aspects* **2004,** *242* (1-3), 93-104.

56. Singh, K. K.; Rastogi, R.; Hasan, S. H., Removal of Cr(VI) from wastewater using rice bran. *J Colloid Interface Sci* **2005,** *290* (1), 61-8.

57. Selatnia, A.; Boukazoula, A.; Kechid, N.; Bakhti, M. Z.; Chergui, A.; Kerchich, Y., Biosorption of lead (II) from aqueous solution by a bacterial dead Streptomyces rimosus biomass. *Biochemical Engineering Journal* **2004,** *19* (2), 127-135.

58. Urano, K.; Tachikawa, H., Process development for removal and recovery of phosphorus from wastewater by a new adsorbent. 1. Preparation method and adsorption capability of a new adsorbent. *Industrial & Engineering Chemistry Research* **1991,** *30* (8), 1893-1896.

59. Tunali, S.; Akar, T.; Özcan, A. S.; Kiran, I.; Özcan, A., Equilibrium and kinetics of biosorption of lead(II) from aqueous solutions by Cephalosporium aphidicola. *Separation and Purification Technology* **2006,** *47* (3), 105-112.

60. Ahalya, N.; Kanamadi, R. D.; Ramachandra, T. V., Biosorption of chromium (VI) from aqueous solutions by the husk of Bengal gram (Cicer arientinum). *Electronic Journal of Biotechnology* **2005,** *8* (3), 258-264.

61. Jafari Behbahani, T.; Behbahani, Z., A new study on asphaltene adsorption in porous media. *Petroleum and Coal* **2014,** *56*, 459-466.

62. Podder, M. S.; Majumder, C. B., Studies on the removal of As(III) and As(V) through their adsorption onto granular activated carbon/MnFe2O4 composite: isotherm studies and error analysis. *Composite Interfaces* **2016,** *23* (4), 327-372.

63. Jeppu, G. P.; Clement, T. P., A modified Langmuir-Freundlich isotherm model for simulating pH-dependent adsorption effects. *J Contam Hydrol* **2012,** *129-130*, 46-53.

64. Travis, C. C.; Etnier, E. L., A Survey of Sorption Relationships for Reactive Solutes in Soil. *Journal of Environmental Quality* **1981,** *10* (1), 8-17.

65. Elmorsi, T. M., Equilibrium Isotherms and Kinetic Studies of Removal of Methylene Blue Dye by Adsorption onto Miswak Leaves as a Natural Adsorbent. *Journal of Environmental Protection* **2011,** *02* (06), 817-827.

66. Chen, C., Evaluation of Equilibrium Sorption Isotherm Equations. *The Open Chemical Engineering Journal* **2013,** *7* (1), 24-44.

67. Tóth, J., State Equation of the Solid-Gas Interface Layers. *Acta Chimica (Academiae Scientiarum) Hungaricae* **1971,** *69*, 311-317.

68. Jeguirim, M.; Dorge, S.; Loth, A.; Trouvé, G., Devolatilization Kinetics of Miscanthus Straw from Thermogravimetric Analysis. *International Journal of Green Energy* **2010,** *7* (2), 164-173.

69. Sing, K. S. W., Reporting physisorption data for gas/solid systems with special reference to the determination of surface area and porosity (Provisional). *Pure and Applied Chemistry* **1982,** *54* (11), 2201-2218.

70. Lizzio, A.; DeBarr, J., Effect of surface area and chemisorbed oxygen on the SO_2 adsorption capacity of activated char. *Fuel* **1996,** *75* (13), 1515-1522.

71. Nguyen, T. H.; Brown, R. A.; Ball, W. P., An evaluation of thermal resistance as a measure of black carbon content in diesel soot, wood char, and sediment. *Organic Geochemistry* **2004,** *35* (3), 217-234.

72. Brateck, K.; Bratek, W.; Kulazynski, M., Carbon adsorbents from waste ion-exchange resin. *Carbon* **2002,** *40* (12), 2213-2220.

73. Luo, W.; Wang, B.; Heron, C. G.; Allen, M. J.; Morre, J.; Maier, C. S.; Stickle, W. F.; Ji, X., Pyrolysis of cellulose under ammonia leads to nitrogen-doped nanoporous carbon generated through methane formation. *Nano Lett* **2014,** *14* (4), 2225-9.

74. Liu, J.; Liu, C.; Zhang, L.; Liu, C.; Cheng, S.; Chandrasekar Srinivasa, K., Preparation of activated carbon from spent catalyst with mercury by microwave-induced CO_2 activation. *Asia-Pacific Journal of Chemical Engineering* **2018,** *14* (1).

75. Quach, N. K. N.; Yang, W.-D.; Chung, Z.-J.; Tran, H. L., The Influence of the Activation Temperature on the Structural Properties of the Activated Carbon Xerogels and Their Electrochemical Performance. *Advances in Materials Science and Engineering* **2017,** *2017*, 1-9.

76. Zhu, J.; Deng, B.; Yang, J.; Gang, D., Modifying activated carbon with hybrid ligands for enhancing aqueous mercury removal. *Carbon* **2009,** *47* (8), 2014-2025.

77. Liu, C.-L.; Dong, W.; Cao, G.; Song, J.; Liu, L.; Yang, Y., Capacitance Limits of Activated Carbon Fiber Electrodes in Aqueous Electrolyte. *Journal of The Electrochemical Society* **2008,** *155* (1).

국문 초록

축전식 이온 제거를 위한 거대억새 유래 다공성 바이오탄소의 제조 및 특성 평가

이영필

지도교수 : 이재욱

화학공학과

조선대학교 대학원

최근 바이오매스 자원(타마린드 껍질, 대추 씨, 솔방울, 오렌지 껍질, 콩 껍질, 아몬드 껍질, 커피 찌꺼기, 코코넛 껍질, 올리브 씨, 밀짚 등)은 탄화 및 활성화 공정을 통해 다공성 바이오탄소 제조에 이용되고 있다. 석탄 계열의 활성탄에 비해 바이오탄소는 수처리, 이산화탄소 포집, 에너지 저장, 센서, 촉매 및 축전식 이온 제거 등 다양한 분야에서 경제적이고 환경 친화적인 탄소 물질로 이용되고 있다.

본 연구에서는 높은 비표면적과 균일한 세공 크기 분포를 갖는 거대억새 유래 다공성 바이오탄소를 성공적으로 제조하였다. 활성화 공정은 상대적으로 낮은 활성화 온도, 타르 생성의 억제, 표면 친수성 향상의 장점을 갖는 $ZnCl_2$ 함침법을 이용한 간단한 단일 공정으로 진행하였다. 최적의 $ZnCl_2$/거대억새 비(1, 2, 4)와 활성화 온도(600, 700, 800 ℃)는 전기화학적 축전용량 및 이온 흡착량에 근거하여 결정되었다. 제조된 바이오카본의 표면 형태, 비표면적, 세공 크기 분포, 결정성을 포함한 물리/화학적 특성평가를 위해 TGA, SEM, BET, XRD, Raman, FTIR 등의 기기분석을 수행하였다. 제조된 다공성 바이오탄소들의 질소 흡/탈착 곡선은 IUPAC에서 정의한 type I의 경향을 보였고, 비표면적 및 평균 세공 크기는 각각 994 – 1661 $m^2 g^{-1}$ 와 약 2 ㎚ 였다. 더불어 거칠기 및 세공 구조들의 발달을 의미하는 D 밴드와 G 밴드의 강도 비는 $ZnCl_2$/거대억새 비와 활성화 온도에 비례하여 증가하였다. 한편 전기화학적 특성은 순환전압전류법, 시간대전류법,

임피던스 분광법을 통해 평가하였으며, 그 결과 비축전용량은 5 mV s⁻¹ 의 주사 속도에서 167 – 228 F g⁻¹ 의 결과를 보였다. 주요 공정변수(유량, 인가 전압, 처리수 농도)에 따른 흡착 및 탈착 곡선은 우수한 재현성을 보였으며, 2000 mg L⁻¹ NaCl 농도 및 1.2 V 조건에서 최대 21.9 mg g⁻¹ 의 이온 흡착량을 보였다. 흡착공정의 특성을 조사하기 위해 다양한 속도 모델(pseudo-frist-order, pseudo-second-order, Weber-Morris, Urano-Tachikawa, S-shape) 및 흡착 평형 모델(Langmuir, Freundlich, Toth, Sips)을 사용하였으며, 그 중 S-shape 속도 모델 및 Sips 흡착등온식이 흡착 속도 및 평형 결과를 잘 묘사하였다. 더불어 상업용 활성탄(CEP21KS)에 비해, 거대억새 유래 다공성 바이오탄소는 높은 비표면적과 잘 발달된 세공 구조특성으로 인해 우수한 이온 흡착량 및 전기화학적 성능을 보였다. 본 연구에서 확보한 기초적인 축전식 이온 제거 연구결과는 향후 태양 에너지, 역삼투막, 정밀 여과, 미생물 연료전지 및 광촉매 분야와 결합된 복합 축전식 이온 제거 공정에 활용 가능성이 클 것으로 전망된다.